Pion generalized parton distributions: A path toward phenomenology

José Manuel Morgado Chávez,[1,*] Valerio Bertone,[2,†] Feliciano De Soto Borrero,[3,‡] Maxime Defurne,[2,§] Cédric Mezrag,[2,‖] Hervé Moutarde,[2,¶] José Rodríguez-Quintero,[1,**] and Jorge Segovia[3,††]

[1]*Department of Integrated Sciences and Center for Advanced Studies in Physics, Mathematics and Computation, University of Huelva, E-21071 Huelva, Spain*

[2]*Irfu, CEA, Université Paris-Saclay, F-91191 Gif-sur-Yvette, France*

[3]*Departamento de Sistemas Físicos, Químicos y Naturales, Universidad Pablo de Olavide, E-41013 Sevilla, Spain*

(Received 29 October 2021; accepted 18 January 2022; published 17 May 2022)

We introduce a new family of generalized parton distribution models able to fulfill by construction all the theoretical properties imposed by QCD. These models are built on standard parton distribution functions and extended to off-forward kinematics through a well-defined procedure. We apply this strategy on the pion, first handling a simple but insightful algebraic model, and then exploiting state-of-the-art computations obtained in continuum QCD. We compare these models with a more standard one relying on an xFitter extraction of the pion parton distribution functions. The results for both quark and gluon generalized parton distributions are presented and exploited for calculation of electromagnetic, gravitational, and Compton form factors. Results on the latter highlight the relevance of next-to-leading-order corrections, even in the so-called valence region.

DOI: 10.1103/PhysRevD.105.094012

I. INTRODUCTION

Generalized parton distributions (GPDs) were introduced more than two decades ago [1–5] and have been deeply studied both theoretically and experimentally since then (see, e.g., the review papers [6–8]). Besides the fact that they allow us to describe multiple exclusive processes such as deeply virtual Compton scattering (DVCS) or deeply virtual meson production (DVMP), the scientific interest for GPDs is fueled both by the access they offer to the three-dimensional picture of hadrons (tomography) [9] and by their connection with the energy-momentum tensor [3]. The latter allows in principle an experimental access to the spin decomposition of hadrons on the one hand, and to the pressure and shear forces of partons inside hadrons [10] on the other hand.

As interesting as they are, GPDs are notoriously difficult both to extract from experimental data and to compute using nonperturbative techniques. On the experimental side, exclusive processes related to GPDs are challenging to measure precisely due to the requirement that the hadronic target should not break and therefore requires a high luminosity. This has consequences on GPD phenomenology, as for spin-$1/2$ targets, the number of independent observables is usually not large enough to properly constrain all amplitudes coming from the different GPDs allowed. This problem is thought to be tamed on spin-0 targets, leading to studies of exclusive processes on ^{4}He targets. Nevertheless, irrespective of the target's spin, the main channels accessible experimentally do not allow by themselves for an unambiguous extraction of GPDs [11,12]. This emphasizes the need of nonperturbative QCD computations of GPDs. Concerning the pion, the phenomenology of parton distribution functions (PDFs) has been maturing in the past few years [13–16], but the phenomenology of GPDs remains to be built.

On the theoretical side, two ways are mainly used today to compute GPDs: lattice QCD and continuum Schwinger methods (CSMs). Following the emergence in the last decade of techniques allowing us to extrapolate Euclidean results onto the light front [17–20] (see also Refs. [21–24]), lattice QCD practitioners have managed to provide information on the shape of parton distribution functions beyond the computations of their first Mellin moments. Attempts to apply these techniques to GPDs are still ongoing, the first results at vanishing skewness on the pion being encouraging [25,26].

*josemanuel.morgado@dci.uhu.es
†valerio.bertone@cea.fr
‡fcsotbor@upo.es
§maxime.defurne@cea.fr
‖cedric.mezrag@cea.fr
¶herve.moutarde@cea.fr
**jose.rodriguez@dfaie.uhu.es
††jsegovia@upo.es

However, going beyond vanishing skewness remains extremely challenging due to the set of theoretical constraints that GPDs need to obey [27]. Nevertheless, lattice QCD is certainly a promising path to be followed in the future.

The last decade was also very fruitful for CSM practitioners on the path to computing GPDs. After early attempts using diagrammatic representations [28–31], the path through light-front wave functions (LFWFs) opened the possibility to obtain GPDs fulfilling all the required theoretical properties [32,33]. However, if a proof of principle has been achieved, the most refined continuum techniques remain to be used in the case of GPDs. Nonetheless, they have very recently been used to evaluate consistently both the pion's parton distribution amplitude (PDA) and PDFs [34,35] (see also Ref. [36] for a review of recent results on the pion), and the first steps toward GPDs have been undertaken [37–39].

Among hadrons, the pion has been one of the main topics of CSM studies for several reasons: (i) It presents the characteristic of being both a QCD bound state and a Goldstone boson of chiral symmetry. (ii) Because of this double role, a description consistent with experimental data requires a proper treatment of symmetries [40], making it an ideal test ground for new techniques. (iii) Presenting a two-body leading Fock state, it remains simpler in some aspects than the nucleon. These CSM studies have contributed to push forward experimental studies such as the extraction of electromagnetic form factors (EFFs) at large momentum transfer, or the pion PDF through tagged deep inelastic scattering (tDIS) (see, e.g., Ref. [41]).

In view of this renewed experimental interest, especially in the perspective of future electron-ion colliders in the USA (EIC) and in China (EicC), we present in this paper the first CSM-based pion-GPD model able to fulfill by construction all the required theoretical constraints. In order to make it relevant for phenomenological purposes, we take advantage of state-of-the-art pion PDF computations based on CSMs, together with the latest experimental extractions of EFFs [42] and gravitational form factors (GFFs) [43]. We compare this model with more standard approaches based on the Radyushkin double distribution *Ansatz* (RDDA) [44]. Thus, we start in Sec. II by recalling the set of theoretical constraints that GPDs have to obey and their consequences. In Sec. III, we present our modeling strategy in a general fashion, and we exploit it to develop two pion-GPD models within the DGLAP (Dokshitzer-Gribov-Lipatov-Altarelli-Parisi) region, one of which is based on the PDF of Ref. [34]. In Sec. IV, we present our way to extend the model to the ERBL (Efremov-Radyushkin-Brodsky-Lepage) region, improving the numerical techniques introduced in Ref. [32]. Section V is devoted to the development of a RDDA-based phenomenological model. Finally, in Sec. VI, we compute and discuss DVCS Compton form factors (CFFs) at next-to-leading order (NLO) using the three models presented.

II. DEFINITION AND PROPERTIES OF GPDs

In this section, we remind the reader of the definition of the pion GPDs and present all the properties they should fulfill together with their consequences.

A. Definition and properties

GPDs are defined from the Fourier transform of nonlocal hadronic matrix elements. Their number depends on the spin of the considered hadron. For the pion, which will be our main focus throughout this paper, one has [6]

$$H_\pi^q(x,\xi,t) = \frac{1}{2}\int \frac{d\lambda}{2\pi} e^{ix\lambda}\langle p'|\bar{\psi}^q\left(-\frac{\lambda n}{2}\right)\not{n}\psi^q\left(\frac{\lambda n}{2}\right)|p\rangle, \quad (1)$$

$$H_\pi^g(x,\xi,t) = \int \frac{d\lambda}{2\pi} e^{ix\lambda}\langle p'|G_\alpha^\mu\left(-\frac{\lambda n}{2}\right)G_\mu^\beta\left(\frac{\lambda n}{2}\right)|p\rangle n^\alpha n_\beta, \quad (2)$$

where ψ^q is a quark field of a given flavor q; $G^{\mu\nu}$ is the gluon field strength, and n is a lightlike four-vector normalized such that $n\cdot P = 1$ with $P = (p+p')/2$. Note that for brevity, we have omitted the dependence on the renormalization scale μ, controlled by evolution equations, and the expression of the Wilson line. The average momentum fraction carried by the active parton is labeled x. The skewness $\xi = [(p-p')\cdot n]/[(p'+p)\cdot n]$ corresponds to the momentum fraction exchanged along the light cone, and t stands for the standard Mandelstam variable.

GPDs are defined for $x \in [-1,1]$ [45] and $\xi \in [-1,1]$. Continuation to $\xi \in [1,\infty)$ is possible through generalized distribution amplitudes thanks to crossing symmetry [46,47]. Time reversal invariance and Hermiticity guarantee that pion GPDs are real functions and even in ξ [6,7].

In the forward limit—i.e., when both ξ and t vanish—GPDs reduce to parton distribution functions:

$$H^q(x,0,0) = q(x)\Theta(x) - \bar{q}(-x)\Theta(-x), \quad (3)$$

$$H^g(x,0,0) = xg(x)\Theta(x) - xg(-x)\Theta(-x), \quad (4)$$

where Θ is the Heaviside distribution, $q(x)$ is the quark PDF of flavor q, $\bar{q}(x)$ is the antiquark PDF, and $g(x)$ is the gluon PDF.

Beyond the forward limit, PDFs also constrain the GPDs at nonvanishing ξ through the so-called positivity bounds. The latter come from the underlying Hilbert-space structure and, in the case of the pion, state that [48–51]

$$|H_\pi^q(x,\xi,t)| \le \sqrt{q(x_{\rm in})q(x_{\rm out})}, \quad (5)$$

$$|H_\pi^g(x,\xi,t)| \le \sqrt{(1-\xi^2)}\sqrt{x_{\rm in}x_{\rm out}g(x_{\rm in})g(x_{\rm out})}, \quad (6)$$

with

$$x_{\text{in}} = \frac{x+\xi}{1+\xi}, \qquad x_{\text{out}} = \frac{x-\xi}{1-\xi} \tag{7}$$

in the DGLAP (or outer) kinematic region ($|x| \geq |\xi|$). Such a property has been shown to be stable under leading logarithm evolution [52].

Because of the historical difficulty in fulfilling both at the same time, the positivity property is usually put in parallel to another important property called polynomiality. It follows as a direct consequence of Lorentz invariance and states that the Mellin moments of GPDs are polynomials in ξ [53–55]:

$$\int_{-1}^{1} dx x^n H^q(x,\xi) = \sum_{i=0}^{[n/2]} (2\xi)^{2i} A^q_{n+1,2i} + \text{mod}\ (2,n)(2\xi)^{n+1} C^q_{n+1}, \tag{8}$$

$$\int_0^1 dx x^{n-1} H^g(x,\xi) = \sum_{i=0}^{[n/2]} (2\xi)^{2i} A^g_{n+1,2i} + (2\xi)^{n+1} C^g_{n+1}, \tag{9}$$

where, in the gluon case, n is always odd, as the gluon-GPD is even. Here, the brackets [] represent the "floor function." We note also that in the case $n = 0$, the Mellin moment of the quark GPD yields the pion's EFF.

Even if GPDs are matrix elements encoding nonperturbative information on the hadron's structure, perturbative QCD (pQCD) still provides us with constraints on GPDs. We highlight here the pion's GPD behavior when $x \to 1$ [56]:

$$H^q_\pi(x,\xi,t) \sim \frac{(1-x)^2}{1-\xi^2}. \tag{10}$$

Furthermore, when $-t$ becomes large, GPDs can be expressed in terms of a convolution of distribution amplitudes with perturbative kernels [57], generalizing the seminal results of the electromagnetic form factor [58,59]. Up to logarithmic corrections, one obtains

$$H^q(x,\xi,t) = \frac{1}{-t} f^q(x,\xi,\alpha_{\text{S}}(t)), \tag{11}$$

where α_s is the strong coupling constant and $f^q(x,\xi,\alpha_{\text{S}}(t))$ simply labels the limit $\lim_{-t\to\infty} -tH(x,\xi,t)$ (see, e.g., Ref. [60] for an extensive discussion in the case of the pion form factor).

Finally, pQCD also constrains mathematical properties of GPDs through their connections with experimental processes. Sometimes called the "golden GPD channel", the amplitude of DVCS can be factorized in terms of coefficient functions, calculable in perturbation theory, and GPDs [5,61,62]. Yet, the factorized amplitude is finite only if the GPDs are continuous on the line $x = \pm\xi$ (this is also true for other processes). At this point, considering the GPDs as a hadron-parton scattering amplitude, Collins and Freund [61] showed that the latter needs to be continuous, but nonanalytic, on the lines $x = \pm\xi$. This is compatible with the one-loop evolution equations (see, e.g., Ref. [63]).

Last but not least, since our study is focused on pion GPDs, we must mention the so-called soft-pion theorem [30,64]. This property tells us that

$$H^q_\pi(x,1,0) = \frac{1}{2}\varphi_\pi\left(\frac{1+x}{2}\right), \tag{12}$$

where φ_π is the leading-twist pion PDA.

The list above sheds light on the properties obeyed by GPDs. One should note that before the present paper, no realistic model was able to fulfill all these constraints by construction. Attempts were developed in low-energy chiral models [65,66]. The first lattice computation at nonvanishing ξ [27] also fails to do so, as the support, continuity and large-x behavior properties are violated in such a pioneering computation.

B. Double distributions

Among all the GPD theoretical properties enumerated above, polynomiality holds a special place. Indeed, introducing an odd function $D(z)$ for $z \in [-1,1]$, called the D-term, such that

$$\int_{-1}^{1} dz z^n D(z) = \text{mod}\ (2,n) 2^n C_{n+1}, \tag{13}$$

one can show [32] that, for each t, the function $H(x,\xi) - \text{sign}(\xi) D(x/\xi)$ fulfills the Lugwig-Helgason consistency condition [67] (called the Cavalieri condition in Ref. [68]), meaning that $H - D$ is in the range of the Radon transform. More precisely,

$$\begin{aligned} H(x,\xi) &= \text{sign}(\xi) D\left(\frac{x}{\xi}\right) + \int d\Omega F(\beta,\alpha)\delta(x-\beta-\xi\alpha) \\ &= \int d\Omega [F(\beta,\alpha) + \xi\delta(\beta) D(\alpha)]\delta(x-\beta-\xi\alpha), \end{aligned} \tag{14}$$

with $d\Omega = d\beta d\alpha \Theta(1-|\beta|-|\alpha|)$. The reader may recognize the double distribution (DD) introduced by Radyushkin [5] (also called spectral functions in Ref. [1]),

$$H(x,\xi) = \int d\Omega [F(\beta,\alpha) + \xi G(\beta,\alpha)]\delta(x-\beta-\alpha\xi), \tag{15}$$

in the so-called Polyakov-Weiss scheme [55], where G is reduced to the D-term times a Dirac delta.

The relation in Eq. (15) between DDs and GPDs is scheme independent (see Ref. [32] for a detailed description). For instance, in the P scheme [69] (which will be useful in later sections), F and G DDs are redefined as

$$F(\beta,\alpha) = (1-|\beta|)h_p(\beta,\alpha), \tag{16}$$

$$G(\beta,\alpha) = -\text{sign}(\beta)\alpha h_p(\beta,\alpha), \tag{17}$$

where h_p is often called a DD by abuse of terminology. The reader interested in the formulas allowing us to go from one scheme to another is referred to Ref. [32] and references therein.

We highlight that, from DDs in any scheme, one can recover two scheme-independent quantities, the PDF $q(x)$ and the so-called D-term, through

$$q(\beta) = \int_{-1+|\beta|}^{1-|\beta|} \mathrm{d}\alpha F(\beta,\alpha), \tag{18}$$

$$D(\alpha) = \int_{-1+|\alpha|}^{1-|\alpha|} \mathrm{d}\beta G(\beta,\alpha). \tag{19}$$

The theoretical constraints fulfilled by GPDs find their analogues when handling DDs. The parity in ξ becomes parity in α, the DD's support guarantees the GPD's support, and the continuity on the $|x| = |\xi|$ lines is embedded in the behavior of the DDs at the points $(\beta,\alpha) = (0,\pm 1)$. Apart from a seminal paper on the topic [69], little work has been done on expressing the positivity property in the DD space. Nevertheless, this does not preclude exploiting DDs in order to build GPD models fulfilling by construction all the required theoretical properties, as we will see below.

III. MODELING THE DGLAP REGION OF THE PION GPDs

Following previous results showing how to exploit the Radon transform relation between GPDs and DDs, we adopt the so-called covariant extension strategy [32,33] to develop a brand-new program for modeling pion GPDs fulfilling all of the fundamental properties required by the underlying quantum field theory (see Sec. II A). It consists in modeling the GPDs within the DGLAP region in such a way that the positivity property is fulfilled. Then, the use of the inverse Radon transform allows us to obtain the associated DD and consequently build the inner (or ERBL) region ($|x| \leq |\xi|$) through the Radon transform [see Eq. (15)]. The polynomiality property of the resulting GPD is therefore guaranteed by construction.

In this section, we focus on the first step of this procedure, presenting a general approach for the modeling of DGLAP quark GPDs with a built-in positive character. We exploit it to develop a whole new family of DGLAP GPDs and illustrate it with an alternative derivation of the algebraic model presented in Ref. [33], which we extensively use as a benchmark. Finally, we introduce a brand-new GPD model based on forefront CSM studies.

A. General framework

Among the possible ways of fulfilling the positivity property when modeling GPDs, we choose to exploit the overlap of light-front wave functions [6,50], for two main reasons: (i) It provides a desirable probabilistic interpretation, similarly to nonrelativistic quantum mechanics [50,70–72], and (ii) nonperturbative computations of these LFWFs have been performed using different techniques, providing, at least in principle, a connection to QCD. However, a difficulty arises: namely, that the type of overlap varies with the kinematical regions. Only the DGLAP region can be described through an overlap of LFWFs with the same number of partons. There, the overlap has the structure of a scalar product in a Hilbert space, guaranteeing by construction the fulfillment of the positivity property [50].

LFWFs depend on two types of kinematic variables: x_i, representing the longitudinal momentum fraction of the hadron's average lightcone momentum carried by a given parton; and $\vec{k}_i^{\perp}$, its momentum in the transverse plane (defined with respect to the hadron's momentum in the infinite-momentum frame). In addition, they depend on a renormalization scale, μ.

Longitudinal momentum fractions for each active parton are defined in Eq. (7). Transverse momentum are defined analogously:

$$\vec{k}_{\text{out}}^{\perp} = \vec{k}_{\perp} + (1-x_{\text{out}})\frac{\vec{\Delta}_{\perp}}{2}, \tag{20}$$

$$\vec{k}_{\text{in}}^{\perp} = \vec{k}_{\perp} - (1-x_{\text{in}})\frac{\vec{\Delta}_{\perp}}{2}, \tag{21}$$

with $\vec{\Delta}_{\perp}$ being the momentum transfer in the hadron's transverse plane.

A complete description of GPDs using LFWFs requires the knowledge of an infinite set of the latter. Thus, the path to GPD modeling from LFWFs requires assumptions. The one we choose is to truncate the pion state's Fock-space expansion to its leading component. We assume that, at a low enough energy scale, a description of hadrons in terms of valence dressed quarks (not partons) is a reasonable approximation, which could, in principle, be systematically improved using LFWFs of higher numbers of dressed quarks and gluons. Under such an assumption, the infinite sum involved in the overlap representation of GPDs for a meson can be truncated to its first term:

$$H_h^q(x,\xi,t;\mu_{\text{Ref.}})|_{|x|\geq|\xi|} = \int \frac{d^2k_{\perp}}{16\pi^3} \Psi^*_{q/h}(x_{\text{out}},\vec{k}_{\text{out}}^{\perp};\mu_{\text{Ref.}})\Psi_{q/h}(x_{\text{in}},\vec{k}_{\text{in}}^{\perp};\mu_{\text{Ref.}}), \tag{22}$$

with Ψ labeling the two-body LFWFs, and where a sum over flavor, helicity, and color states is implicitly

understood. Such a truncation preserves the structure of the Hilbert space, conserving therefore the positivity property.

The reader may argue that the computation of such valence LFWFs for mesons is already a hard task by itself. There are different ways to proceed—maybe the easiest course to obtain a description in terms of effective particles is the covariant treatment of the corresponding quantum-field theoretical bound-state equations [40,73–76] and its projection onto the light front.

In this respect, recent studies [38,39,77] suggest that the use of factorized *Ansätze* for LFWFs provides a fair approximation to the description of nonperturbative hadronic features that may be difficult to grasp from first-principle calculations. In particular, the factorization hypothesis has proven to yield a good approximation in the description of pions [77]. Thus, as far as we are concerned with a phenomenological study of pions, considering such an approach deserves special attention.

Therefore, we consider the leading-twist two-particles—e.g., π LFWFs for a pair of quarks of flavor (q_1, q_2) and of helicity (λ_1, λ_2):

$$\Psi^{\lambda_1\lambda_2}_{q_1q_2/\pi}(x, \vec{k}_\perp) = f_{q_1q_2/\pi}(x) g^{\lambda_1\lambda_2}_{q_1q_2/\pi}(k^2_\perp), \tag{23}$$

where a sum of color degrees of freedom is understood. For simplicity in the notation, we have omitted any explicit reference to the renormalization scale $\mu_{\text{Ref.}}$.

Our truncation requires the LFWF in Eq. (23) to satisfy the sum rule,

$$q_\pi(x) = \sum_{\substack{\lambda_1,\lambda_2\\ q_1,q_2}} \delta_{qq_1} \int \frac{d^2k_\perp}{16\pi^3} |\Psi^{\lambda_1\lambda_2}_{q_1q_2/\pi}(x, \vec{k}_\perp)|^2, \tag{24}$$

with $q_\pi(x)$ being the leading-twist quark PDF.

One can build a simple *Ansatz* for $f_{q_1q_2/\pi}$ in order to fulfill Eq. (24):

$$f_{q_1q_2/\pi}(x) = \sqrt{q_\pi(x)}, \tag{25}$$

and therefore, employing the formalism of the overlap representation, build two-particle bound-state DGLAP GPDs. Plugging Eq. (25) into Eq. (22), one gets [39]

$$H^q_\pi(x, \xi, t)|_{x\geq|\xi|} = \sqrt{q_\pi(x_{\text{in}}) q_\pi(x_{\text{out}})} \Phi^q_\pi(x, \xi, t), \tag{26}$$

which defines the "master equation" for our modeling strategy. As mentioned above, we expect this equation to be in fair agreement with the one coming from an overlap of the full LFWFs including nonfactorizable terms [38,39,77].

The above relation defines a whole new family of DGLAP GPDs, built on a basis of parametrizations for the corresponding hadron PDFs. Furthermore, its momentum-transfer dependence is encoded into a single function,

$$\Phi^q_\pi(x, \xi, t) = \sum_{\substack{\lambda_1,\lambda_2\\ q_1,q_2}} \delta_{qq_i} \int \frac{d^2k_\perp}{16\pi^3} g^{\lambda_1\lambda_2^*}_{q_1q_2/\pi}(k^{\perp 2}_{\text{in}}) g^{\lambda_1\lambda_2}_{q_1q_2/\pi}(k^{\perp 2}_{\text{out}}), \tag{27}$$

which can be directly obtained from separable *Ansätze* for LFWFs. As a final remark, notice that from such an expression, one might expect the variables x, ξ, and t to be correlated, as indicated by both theoretical considerations [78] and lattice studies [79]. This will turn out to be one of the main features exhibited in the GPD models presented here.

Interestingly, the canonical normalization [Eq. (24)] of the LFWF [Eq. (23)] requires that $\Phi^q_\pi(x, \xi, t = 0) = 1$, and therefore one trivially gets

$$H^q_\pi(x, \xi, 0) = \sqrt{q_\pi(x_{\text{in}}) q_\pi(x_{\text{out}})}, \tag{28}$$

revealing an interesting property of the present modeling strategy: GPDs built under the assumption of LFWF factorization *saturate* the positivity property at vanishing t.

Finally, let us highlight that the present model provides a flexible and valuable new way to model GPDs at low scale through PDFs, which are usually well-known quantities (although not much in the case of the pion). In addition, if the t dependence is "factorized out" of the PDF's dependence, it remains intertwined with the momentum fraction x and ξ. This is again an interesting alternative to the models presenting a fully factorized t dependence.

B. Pion GPDs

As mentioned above, obtaining the valence LFWFs is a research topic by itself. Different approaches can be envisioned, like light-front basis techniques or AdS/QCD [80–82]. In this work, we will focus on the CSM approach [83,84], briefly describing how the LFWFs can be obtained from the Bethe-Salpeter wave function (BSWF). The latter is the solution of the so-called Bethe-Salpeter equation [83,84], describing bound states in a covariant way. Interestingly, one can project the two-body BSWF of mesons on the light front to recover the valence LFWFs.

Light-front projection is unfortunately not that simple, mainly because using CSMs, the solutions are obtained using a Euclidean metric, meaning that the light cone is reached only in continuing the momentum dependence to the complex plane. This difficulty can be bypassed using the Nakanishi representation [85–87], as exemplified in Ref. [33], following earlier studies [28–31,88–92]. This allows calculations of the pion's quark LFWFs with and without orbital angular momentum, of which we take advantage here.

Indeed, exploiting the results of Ref. [33], and thus taking into account the two independent helicity states of the quarks ($\uparrow\downarrow$ and $\uparrow\uparrow$), we can derive the following expression for the Φ function of Eqs. (26) and (27):

$$\Phi_\pi^q(x,\xi,t) = \frac{1}{4}\frac{1}{1+\zeta^2}\left(3+\frac{1-2\zeta}{1+\zeta}\frac{\operatorname{arctanh}\left(\sqrt{\frac{\zeta}{1+\zeta}}\right)}{\sqrt{\frac{\zeta}{1+\zeta}}}\right), \tag{29}$$

with

$$\zeta = -\frac{t}{4M^2}\frac{(1-x)^2}{1-\xi^2}. \tag{30}$$

Exploring the effect of various models for the pion PDFs may open the door to a large number of pion GPD models built on the basis of simple fundamental assumptions. In this work, we exploit this possibility with two existing parametrizations: a simple one, which has already been reported in Ref. [33] for the study of GPDs; and one further, more sophisticated PDF parametrization based on state-of-the-art CSM approaches to QCD [34].

1. Algebraic PDF parametrization

A first possible parametrization for a quark PDF in a pion was given in Ref. [33], through (see also Fig. 1)

$$q_\pi(x) = 30x^2(1-x)^2. \tag{31}$$

Plugged into Eq. (26), such a PDF straightforwardly yields the GPD (Fig. 2):

$$H_\pi^q(x,\xi,t)|^{\text{Alg.}}_{x\geq|\xi|} = 30\frac{(1-x)^2(x^2-\xi^2)}{(1-\xi^2)^2}\Phi_\pi^q(x,\xi,t), \tag{32}$$

with $\Phi_\pi^q(x,\xi,t)$ given in Eq. (29), and where the mass scale M is fitted to the experimental value of the pion charge radius at a value of $M = (318 \pm 4)$ MeV (see Ref. [33]).

This algebraic parametrization presents the expected large-x behavior, but not the asymptotic $1/t$ decrease. Instead, a $1/t^2$ decrease is obtained due to not taking into account all four components of the Bethe-Salpeter amplitude (BSA) (see, for instance, Refs. [38,39] for an example on how to correct this). Fortunately, since experimental interest in GPDs holds at low values of $|t|$, the algebraic model results should remain relevant to obtaining reasonable experimental yields. In fact, it is able to reproduce well the available data on the pion's electromagnetic form factors, even for $|t|$ above 1 GeV^2 [33].

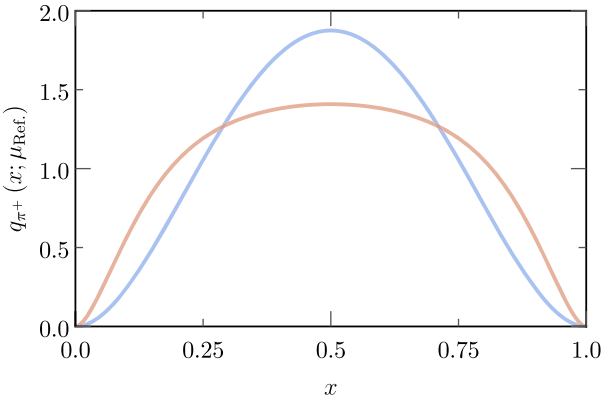

FIG. 1. Comparison between the algebraic u-quark PDF computed in Ref. [33] (blue line) and the one obtained through the solution of the Bethe-Salpeter equation in Ref. [35] (brown line).

2. Numerical PDF parametrization

The quark PDF parametrization giving rise to the GPD model of Eq. (32) is known to fail in the description of dynamical chiral symmetry breaking in QCD [88]. The natural next step is then to employ *Ansätze* accounting for such a fundamental phenomena of QCD.

In particular, we decide to employ the realistic pion PDF presented in Ref. [34]. There, the authors employed a symmetry-preserving truncation scheme for the system of Dyson-Schwinger equations that led them to a numerical solution to the Bethe-Salpeter equation, which, for the case of quark PDFs, yielded

$$q_\pi(x) = \mathcal{N}_q x^2(1-x)^2[1+\gamma x(1-x)+\rho\sqrt{x(1-x)}], \tag{33}$$

with $\mathcal{N}_q = 213.32$, $\gamma = 2.2911$, and $\rho = -2.9342$, defined at a reference scale $\mu_{\text{Ref.}} = 311$ MeV [35]. Notice that such a PDF, as well as that of Eq. (31), exhibits an $x \to 1$ behavior compatible with QCD's parton model prediction [93,94]. Also, because of the two-body approximation, the same behavior appears in the $x \to 0$ limit. This behavior is a consequence of the computations done in Ref. [34], and was not imposed *a priori* as a modeling assumption.

Figure 1 shows a comparison with the simple PDF of Eq. (31). That figure reveals a crucial difference between the two models: owing to dynamical chiral symmetry breaking, the present parametrization exhibits a shape broader than the PDF employed through the previous subsection [34].

Our approach can be extended to the PDF in Eq. (33). The resulting GPD for $0 < \xi < x$ is shown in Fig. 2 together with that of Eq. (32). Two interesting features are revealed: first, both GPD models are manifestly positive within the DGLAP region; next, the shape of the PDF is "transferred" to that of the GPD in the outer subdomain. In that sense, hardening of the GPD's shape within the DGLAP region can be associated with dynamical chiral symmetry breaking, in the sense of Ref. [88].

Interestingly, our models are zero at $x = \xi$. This characteristic behavior arises as a consequence of the end-point behavior of the factorized LFWFs employed for their development. The $x = \xi$ line gives access to a very particular kinematic configuration, where the momentum fraction along the light cone carried by the probed parton in the initial hadron state vanishes. Since the two-body leading-twist LFWF reduces to a two-body leading-twist

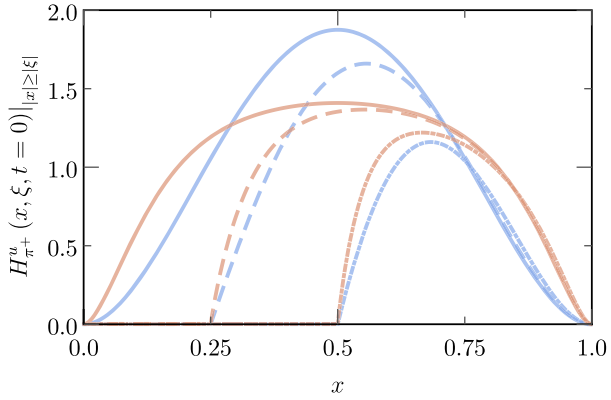

FIG. 2. Shapes of the algebraic (blue lines) and numerical (brown lines) pion u-quark DGLAP GPDs, drawn for $\xi = 0$ (solid), $1/4$ (dashed), and $1/2$ (dot-dashed), and zero momentum transfer.

PDA when integrated over $k_\perp$, it consistently vanishes at the end points [6], in agreement with our findings. It also allows us to avoid mathematical complications [95].

IV. EXTENSION TO THE ERBL REGION

Following the pioneering work in Ref. [96], it was shown in Ref. [32] and confirmed in Ref. [97] that, from a GPD model given in the DGLAP subdomain, it is possible to reconstruct uniquely the ERBL region up to D-term-like contributions. In this section, we sketch the approach followed herein, which relies on a FEM-like (finite element method) strategy to approximate a DD, solve the inverse Radon transform problem to compute such a DD, and employ it to "extend" a GPD from the DGLAP to the ERBL region. We highlight the improvements performed since Ref. [32], where it was first presented.

A. The covariant extension strategy

1. Double distribution schemes

As mentioned in Sec. II B, DDs are "scheme dependent" in the sense that they are not uniquely defined through solely a GPD (see Refs. [32,68,98]). Uniqueness is recovered only when a "scheme" is fixed. The GPD itself remains independent of the scheme chosen. In the present paper, we choose to work within the so-called P-scheme [69] presented in Eqs. (16) and (17). There are several reasons for that. First, this representation was designed in a way which makes it suitable for DD models fulfilling the positivity property. Next, the exact solution to the inverse Radon problem is known for the algebraic model in this specific scheme [33], providing a natural way to benchmark our code. It also requires us only to invert a single function h_p rather than two DDs, F and G, while not introducing additional singularities [32]. We will therefore focus in the following on extracting the function h_p.

2. Discretization and sampling

Discretization of the support domain Ω of DDs introduced in Sec. II B is the first step to carry out before being able to approximate DDs through FEM. This can be done efficiently by taking symmetries into account. The parity in α (see Sec. II B) tells us that we can restrict ourselves to the upper half of the (β,α) plane. Moreover, because of the structure of the Radon transform in Eq. (15), the areas $\beta > 0$ and $\beta < 0$ are probed respectively by "DGLAP lines"—i.e., lines obeying the $x_i - \beta - \alpha\xi_i = 0$ equation such that $|x_i| \geq |\xi_i|$, with the cases $x > 0$ and $x < 0$ not mixing among each other. Since the models described in Sec. III B are identically zero in the negative-x DGLAP region, one can restrict the study without loss of generality to the triangle $\Omega^+ = \{\beta \geq 0\} \cap \{\alpha \geq 0\} \cap \Omega$.

This triangle is then divided into cells through a Delaunay triangulation (chosen for its property of avoiding sliver triangles). We impose a constraint on the maximal possible area of a single element (see Fig. 3). With such a constraint (set through this work as 0.001), the `triangle` discretization algorithm [99] yields a given Delaunay triangulation of the DD support. We end up generating a mesh with 427 vertices (taken as interpolation nodes) and 780 elements. After triangulation, the Radon transform problem of Eq. (15) is reduced to a discrete (matrix) version in the sense of FEM.

Once the Ω^+ domain is discretized, it is embedded with a set of basis functions that allows us to approximate the DD. In this work, these are chosen as two-dimensional degree-one Lagrange polynomials with a restricted domain: P1-polynomials. Then each node is allocated with one such basis function so that three conditions are met: (i) the basis function takes the value 1 at the corresponding node and 0

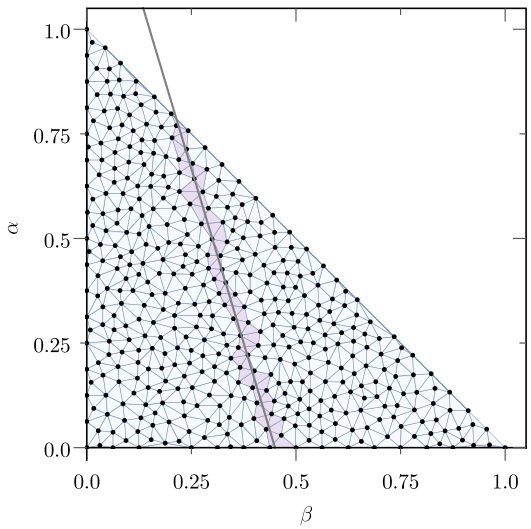

FIG. 3. Delaunay triangulation of the upper-right triangle of the DD support, Ω^+, with an example "DGLAP line" hitting some of the cells. All elements can be sampled by such lines cutting the $\beta = 0$ axis outside of the DD support.

for all others, (ii) its support spreads over the elements adjacent to such a node, and (iii) it vanishes on its external boundaries. In this way, all three defining parameters for each basis function are unambiguously fixed, and the continuity of the DD on the cell edges is ensured (see Ref. [32] for further details).

Finally, since the Radon transform operator of Eq. (15) can be understood as an integral over lines satisfying $x_i - \beta - \alpha\xi_i = 0$, we can choose pairs (x_i, ξ_i) within the DGLAP region, build "DGLAP lines," and thus sample the DD domain (Fig. 3). Through such a sampling process, the Radon transform operator is discretized, and we can build a system of linear equations that faithfully represents the corresponding Radon transform problem:

$$B \equiv (b_i) = (\mathcal{R}_{ij})(d_j), \tag{34}$$

where d_j is the unknown value of the DD (represented by a vector D) at a node, j, of the mesh. $\mathcal{R}$ is the Radon transform matrix, whose (i, j) element represents the contribution of the jth basis function to the approximation of the DD, and $b_i = H(x_i, \xi_i)$ are the elements of the vector B, representing the GPD that must be yielded.

Accessing the ERBL part of a GPD then requires solving the above problem: its solution provides us with the DD associated with the input DGLAP GPD through a Radon transform. Unfortunately, solving such a system of equations may not be straightforward, the reason for that being the *ill-posedness* [100–102] of the inverse Radon transform problem.

For a better understanding, let us delve into the structure of the Radon transform operator. It has been briefly mentioned that, after discretization of Ω^+, its sampling with DGLAP lines allows us to build a discrete version of such an operator: the Radon transform matrix, $\mathcal{R}$. Therefore, accurately sampling such a domain is a crucial step in solving the inverse Radon transform problem. A first possibility in this respect is to choose a number of sampling lines, m, that equals that of the interpolation nodes, n. Thus, one ends up with a squared $\mathcal{R} \in \mathcal{M}_{m\times n}$ matrix. However, the geometry of the DD's domain may prevent that system from having a (unique) solution. In a nutshell, the discretization mesh has most of its nodes located within the low-β region (Fig. 3). For this reason, naively sampling that domain with the minimum possible number of randomly distributed lines may result in an underconstrained system of equations—i.e., Rank $(\mathcal{R}) < n$.

An alternative procedure consists of choosing the sampling lines in a smart way—i.e., such that every node on the mesh is probed by a given line, Rank $(\mathcal{R}) = n$. Then, the entire discrete domain is covered, but a new drawback arises as a consequence of the DD domain's geometry: in order to probe the low-β region, sampling lines with growing slope are needed (Fig. 3); thus, because most of the interpolation nodes are located therein, such a procedure ends up with most of the sampling lines being nearly parallel and grouped within that region. This brings mostly redundant information that would be numerically compatible with infinitely many solutions. Stated differently, many of the sampling lines may yield nearly identical contributions to the same set of interpolation nodes (Fig. 3), resulting in a system of equations whose solution is strongly dependent on the way sampling lines are chosen (initial conditions). In the language of numerical analysis, the system's matrix is *badly conditioned* [103].

Therefore, regarding the discrete version of the inverse Radon transform problem, neither the existence nor the uniqueness of a solution can be granted. Both of them are sufficient conditions for a problem to be *ill-posed* in the sense of Hadamard. Furthermore, the inverse Radon transform operator (even without discretization) is noncontinuous, and thus the stability property of well-posed problems is also violated.

Nevertheless, Lorentz invariance guarantees that physical GPDs are the Radon transform of DDs (see Sec. II B), meaning that a unique solution to the inverse Radon problem must exist. It is the discretization step which may push the GPDs outside of the range of the Radon transform. In fact, this feature is well known in the context of computerized tomography, where the Radon transform is a common tool, and is referred to as an *inconsistent data problem* [102]. Therefore, facing the problem in Eq. (34) requires working out the question of sampling to bypass the inconsistency of the problem at hand.

A possible strategy to deal with such problems is to build an overconstrained system of equations and look for its solution through a least-squares strategy. Such approach can be justified based on the discussion developed immediately before. Clearly, for the system of equations in Eq. (34) to have a unique solution, the condition for maximal rank must be granted. However, we already argued that choosing $m = n$ sampling lines might lead to an inconsistent problem. Fortunately, this situation can be circumvented. To illustrate, let us choose $m = n$ sampling lines in a way such that every interpolation node is sampled at least once. As discussed before, $\mathcal{R}$ has maximal rank; therefore its solution exists and is unique. It is numerical instability which obscures it. Plainly, it is always possible to add a further equation, the resulting matrix being now rectangular but still full rank and with different eigenvalues. Consequently, the $\mathcal{R}$ matrix's singular values are modified, and potentially, its conditioning is improved. This process can be repeated, and thus the condition number of the system's matrix can be progressively improved until stability of the solution is observed, allowing us to reveal the actual DD.

Therefore, for a large enough number of sampling lines, $m > n$, uniqueness of the solution within the numerical precision can be achieved by improving the matrix's conditioning. Moreover, for the sake of flexibility (avoiding mesh-specific sampling algorithms) we choose to randomly

distribute the whole set of sampling lines. In that way, $m \geq 2n$ is empirically found to yield a matrix $\mathcal{R}$ such that Rank $(\mathcal{R}) = n$, whose condition number is small enough for the system's solution to be found, allowing us to overcome the difficulties introduced by the ill-posedness of the inverse Radon transform problem.

3. Normal equations

Provided that the number of sampling lines is large enough, the uniqueness of the solution to the numerical problem is unraveled at the price of dealing with an overconstrained system of equations. In this context, an efficient strategy allowing us to find a solution is to turn to a least-squares formulation.

Naively speaking, in the absence of an exact solution to the overconstrained system at hand, an accurate choice is to look for a solution which deviates less from the actual one. Namely, one can look for the solution D that minimizes:

$$\chi^2 = \frac{1}{\sigma^2_{\mathrm{DGLAP}}} \sum_i (b_i - \mathcal{R}_{ij} d_j)^2, \tag{35}$$

i.e., to search for the DD's values at the interpolation nodes d_j, such that the residual χ^2 is minimized. Note that we have included a constant uncertainty σ_{DGLAP} over the values of the DGLAP region GPD, b_i. Being constant, the uncertainty factor does not impact on the minimization.

In that way, the combination of two main features allows one to deal with the ill-posed inverse Radon transform problem: namely, (i) an overconstrained system of equations, which guarantees existence [Rank $(\mathcal{R}) = n$] of the solution, and (ii) a least-squares approach, granting that the best possible solution [in the sense of Eq. (35)] is found. Furthermore, since polynomiality entails the existence of one single DD related through a Radon transform to a given DGLAP GPD, the solution, found through least-squares optimization of the problem in Eq. (34) defined by a well-enough conditioned matrix $\mathcal{R}$, must be viewed as the actual (best possible) double distribution.

In previous studies of the inverse Radon transform [32], the solution to the problem of Eq. (35) was found by an iterative least-squares algorithm optimized for sparse matrices: the LSMR [104]. In such a context, the residual χ^2 is recursively minimized up to a given tolerance, and thus the solution d_j is obtained.

However, in this work we choose an alternative approach which consists of an exact solution of the optimization problem in Eq. (35). Minimization of the residual with respect to d_k readily yields the solution to such a problem to be given by

$$\mathcal{R}^T \mathcal{R} D = \mathcal{R}^T B, \tag{36}$$

corresponding to the so-called normal equations of the linear system [Eq. (34)], whose solution provides us with a DD such that χ^2 in Eq. (35) is minimized. Note that the system of equations obtained here is the same as the one in Eq. (34) multiplied by the transposed Radon transform matrix, $\mathcal{R}^T$, but the system is now squared, with the size of the matrix $\mathcal{R}^T\mathcal{R}$ being the number of nodes.

For the system above to have a solution, the new system's matrix $(\mathcal{R}^T\mathcal{R})$ must be full rank. Such a condition is satisfied, provided that the Radon transform matrix $\mathcal{R}$ has maximal rank (see the Appendix), a condition which, as discussed throughout the preceding section, is fulfilled by construction. Then, the inverse matrix $(\mathcal{R}^T\mathcal{R})^{-1}$ is proved to exist, and thus the DD which solves the least-squares problem in Eq. (35) is obtained as

$$D = (\mathcal{R}^T\mathcal{R})^{-1}\mathcal{R}^T B. \tag{37}$$

Therefore, the inverse Radon transform problem can be always solved, the DD being found through Eq. (37). The key idea behind it is the overconstrained character of the system of equations. In fact, this idea of adding extra equations to improve the matrix's conditioning (see Sec. IV A 2) can now be seen more intuitively: once the rank of the $\mathcal{R}$ matrix is maximal, adding more lines does not modify the system's size [$\mathcal{R}^T\mathcal{R}$, Eq. (36)]; rather, it produces larger diagonal elements and hence smaller uncertainties, as the covariance matrix is proportional to $(\mathcal{R}^T\mathcal{R})^{-1}$ (see Sec. IV A 4). For this reason, the present method is proved to yield more accurate results than the previously used LSMR method. Furthermore, since matrix-inversion routines are, generally speaking, carefully optimized, the normal equations strategy is also shown to be much more efficient. Therefore, it was adopted for the covariant extension developed within this work.

4. Uncertainty assessment

With the DD obtained through the inverse Radon transform strategy, the ERBL domain can be accessed; one just needs to sample the Ω^+ domain with "ERBL lines"—i.e., choosing pairs $(x_i, \xi_i) \in [-1,1] \otimes [-1,1] \cap \{|x_i| \leq |\xi_i|\}$—to build the corresponding matrix $(\mathcal{R}_{\mathrm{ERBL}})$ and employ it in combination with the DD to evaluate the ERBL GPD at a given point through

$$B_{\mathrm{ERBL}} = \mathcal{R}_{\mathrm{ERBL}} D. \tag{38}$$

One further virtue of the normal equations strategy is that it provides a direct and clear window onto the assessment of the uncertainties originated by discretization and interpolation of the DD. Indeed, when solving the least-squares problem derived from Eq. (35), the covariance (C) matrix of the solutions D is given by $C = \sigma^2_{\mathrm{DGLAP}}(\mathcal{R}^T\mathcal{R})^{-1}$. And solving the inverse Radon transform problem through Eq. (37) requires knowledge of the matrix $(\mathcal{R}^T\mathcal{R})^{-1}$.

The uncertainty of the results of the GPD's covariant extension to the ERBL region can be obtained by applying

standard uncertainty propagation to Eq. (38), and is given by [105]

$$\sigma^2_{\mathrm{ERBL},i} = \sum_{jk} \frac{\partial B_{\mathrm{ERBL},i}}{\partial d_j} \frac{\partial B_{\mathrm{ERBL},i}}{\partial d_k} C_{jk} = \sigma^2_{\mathrm{DGLAP}} (\mathcal{R}_{\mathrm{ERBL}} (\mathcal{R}^T \mathcal{R})^{-1} \mathcal{R}^t_{\mathrm{ERBL}})_{ii}. \quad (39)$$

Therefore, the only ingredient that remains to be estimated is the uncertainty σ_{DGLAP} associated with the DGLAP GPD yielded by our numerically computed DD. Here, we adopt a conservative approach and estimate it as the maximum separation between the input and numerical DGLAP GPDs, $\sigma^2_{\mathrm{DGLAP}} = \max_i (b_i - \sum_j \mathcal{R}_{ij} d_j)^2$. Then, the covariance and $\mathcal{R}_{\mathrm{ERBL}}$ matrices allow us to propagate such an uncertainty to the ERBL region.

5. Soft-pion theorem

After the covariant extension explained above, one is still left with the issue of the D-term ambiguities, as explained in Refs. [32,106]. In order to handle them, we exploit the soft-pion theorem mentioned in Eq. (12). Technically speaking, both x-even and x-odd ambiguities can arise, but since the even one does not play any role in the computation of the CFFs, we will focus on the odd one, that we call the extrinsic D-term. The interested reader can find more details in Refs. [32,33] and references cited therein.

At vanishing momentum transfer, Eq. (12) tells us that the quark GPD needs to be even at all scales—i.e., the singlet and gluon GPDs are vanishing in the limit $(\xi, t) \to (1, 0)$. This condition naturally allows us to fix the extrinsic D-term $D^{q/g}$ at all scales following

$$D^q(z, 0; \mu^2) = -\frac{H^q(z, 1, 0; \mu^2) - H^q(-z, 1, 0; \mu^2)}{2} \quad (40)$$

for quarks, and

$$D^g(z, 0; \mu^2) = -\frac{H^g(z, 1, 0; \mu^2) + H^g(-z, 1, 0; \mu^2)}{2} \quad (41)$$

for gluons.

However, the soft-pion theorem does not provide any information about the t dependence of the D-term. To constrain the latter, we rely on pQCD predictions, stating that at large $-t$, the moments of the pion's GPD behave like $1/|t|$ up to logarithmic corrections [57]. We therefore choose a monopole description using the same mass scale as the one previously advocated:

$$D^{q/g}(z, t; \mu^2) = \frac{D^{q/g}(z, 0, \mu^2)}{1 - \frac{t}{M^2}}, \quad (42)$$

with M already introduced in Eq. (30), and we use it for all quark flavors and gluons.

6. Validation

Once we have presented the general idea behind the covariant extension strategy, we can exploit it for the extension of a given model and thus illustrate its advantages and drawbacks. For this purpose, since its ERBL region is known in closed form [33], the algebraic model pion DGLAP GPD discussed in Sec. III B constitutes an outstanding benchmark, allowing for comparison with the numerical results obtained through the approach presented in the previous sections.

As an illustration, Fig. 4 shows a comparison between the results obtained through the numerical implementation of the covariant extension strategy described before (blue and orange lines) and the actual, analytical result [33] (dashed black line) at $\xi = 1/2$ and $t = 0$.

For this example, the Radon transform matrix was filled by sampling the Ω^+ domain with 3120 "DGLAP lines" (corresponding to 4 times the number of mesh cells, n_e), represented in blue; and 9360 sampling lines ($12n_e$), in orange. Both configurations prove to yield $\mathcal{R}$ matrices of maximal rank. Then the system of equations is solved by means of the normal equations strategy. Together with the numerical solutions, the corresponding error bands are shown (1 standard deviation).

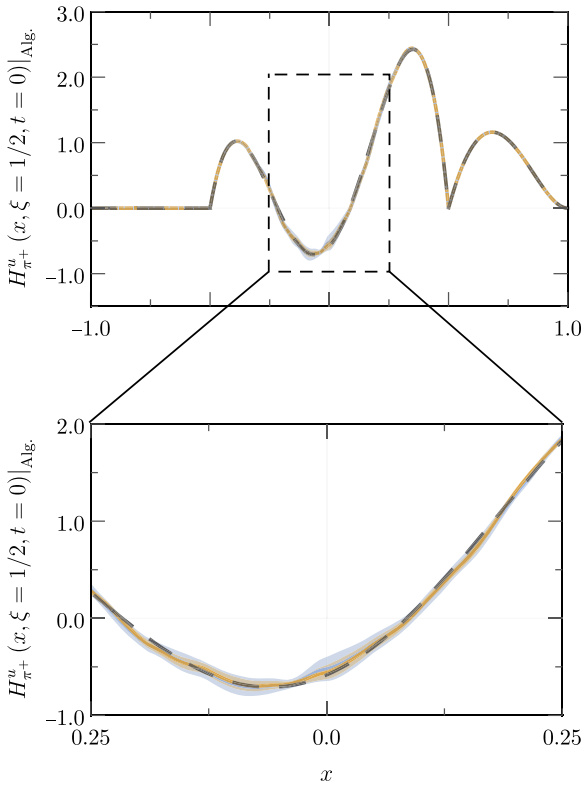

FIG. 4. Algebraic model pion GPD at $\xi = 1/2$ and $t = 0$. Comparison between the exact, analytical result (dashed black line) [33] and two solutions of the associated numerical problem: $\mathcal{R}$ built with 3120 (blue) and 9360 (orange) sampling lines.

From Fig. 4, it is plain that the numerical approach described above yields satisfactory results, the numerical solution being essentially indistinguishable from the analytical result. Only in the inner region can deviations from the actual curve be observed, but even there, the analytical curve is always lying within the corresponding uncertainty band for both numerical solutions. This agreement was verified to remain true for calculations with different configurations (number of sampling lines) and kinematic configurations. From a statistical perspective, we would have expected the analytical results sometimes to be out of the error band. As this is not the case, we deduce that our choice for σ_{DGLAP} is probably too conservative, generating uncertainty bands which are too large. We nevertheless stick to that choice in the following to assess an order of magnitude of the uncertainties generated by the numerical inversion.

Finally, both configurations of the sampling strategy prove to yield nearly identical results; the uncertainty band associated with the solution using a larger number of sampling lines turns out to be narrower at the price of increasing the computation time. This finding was in fact expected, as increasing the number of sampling lines allowed us to build systems' matrices with larger eigenvalues, thus favoring a better performance of the inversion routine for $\mathcal{R}^T\mathcal{R}$. An exhaustive analysis confirmed this observation and showed that the configuration with $12n_e$ randomly distributed sampling lines, which we employ for the rest of this work, represents the optimal compromise between accuracy and performance.

B. Covariant extension of the numerical model

1. Numerical inversion

Once the formalism of the covariant extension has been presented and validated, we apply it for the completion of our two GPD models (Sec. III B). The algebraic one is continued to the ERBL domain following the approach of Ref. [33]—i.e., exactly solving the inverse Radon transform problem. On the other hand, the DGLAP GPD model built from the pion-PDF parametrization of Eq. (33) is extended by means of the numerical procedure developed above.

As an illustration, Fig. 5 shows the resulting GPDs at vanishing t and $\xi = 1/2$. The numerical model exhibits an oscillating behavior within the ERBL region, more marked than that of the algebraic model. Such behavior is confirmed by the conservative assessment of the error band associated with our numerical extraction. Indeed, the error band is large at the top of the oscillation but small around the zero crossings, confirming the oscillating pattern shown by the numerical GPD.

Beyond this oscillating behavior, we stress that the continuity at the crossover lines $|x| = |\xi|$, highlighted in Sec. II A (see also Ref. [61]), is indeed a noticeable outcome, since it has not been imposed, and with the inverse Radon transform not being continuous itself. Interestingly, following other types of model based on DDs (see, e.g., Refs. [44,107]), the first derivative is not continuous. This "singularity" is inherited from the behavior of the DDs on the corners of their definition domain [98], and it is consistent with the LO evolution kernel [63].

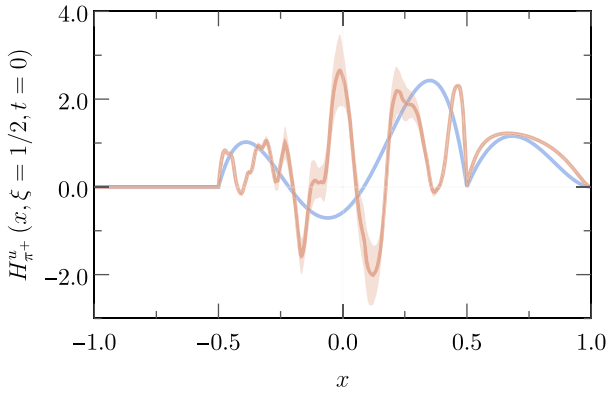

FIG. 5. Algebraic (blue line) and numerical model (brown line) evaluated at vanishing momentum transfer for $\xi = 1/2$ after fixing the D-term ambiguity with the soft-pion theorem.

Last but not least, let us mention that this continuity property is a key point for being able to describe exclusive processes, whose factorization theorem is inconsistent with discontinuous GPDs on the crossover lines. It thus makes the pion GPD models developed here suitable for phenomenological applications, guaranteeing the calculation of CFFs to yield finite results (see Sec. VI B).

2. Electromagnetic and gravitational form factors

Once the GPD models are defined over the entire kinematic domain, they can be exploited for the calculation of Mellin moments, in general, and electromagnetic or gravitational form factors, in particular.

Coming back to Eq. (8), we recall that the pion EFF can be computed for each quark flavor as (see Fig. 6)

$$F^q(t) \equiv A^q_{1,0}(t) = \int_{-1}^{1} dx H^q_\pi(x, \xi, t). \tag{43}$$

Notice that such a Mellin moment does not depend on the skewness variable and thus can be obtained from a direct integration of GPDs as defined in the forward limit (DGLAP GPD with $\xi = 0$). This property allows for a cross-checked calculation of the EFF: both using covariantly extended and forward-limit-only GPDs. As expected, this approach revealed no dependence of the pion EFF on the ERBL completion strategy.

Results obtained for both the algebraic and realistic models show good agreement with available experimental data [42,108–118], especially when $|t| \leq 1$ GeV^2 (Fig. 6), the kinematic region that we are mostly interested in.

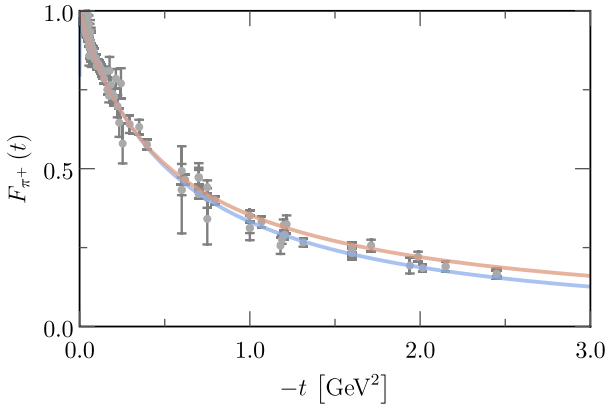

FIG. 6. Calculation of the pion's electromagnetic form factor within the two models discussed through this text: algebraic model (blue line) and numerical model (brown line). Comparison with experimental data from Refs. [42,108–118].

Moreover, such satisfactory results are obtained with one single free parameter: the mass scale M arising in the LFWFs (see Sec. III). It was fitted to the pion's electromagnetic charge radius, $r_\pi = 0.672 \pm 0.008$ fm [119], through

$$r_\pi^2 = -6\frac{F_\pi(-t)}{d(-t)}\bigg|_{t=0} \Rightarrow F_\pi(-t) \simeq 1 - \frac{r_\pi^2}{6}(-t), \tag{44}$$

yielding a value of $M = 318$ MeV for both models. In this sense, the results shown on Fig. 6 can be understood as model predictions for the pion EFF. Getting this accurate fit of experimental data also reveals a deeper implication: the absence of some components of the pion's BSA (e.g., pseudovector components) does not introduce significant deviations from the expected monopole-like behavior (within the explored t range).

With the models at hand, it is possible to go a step forward and compute higher-order Mellin moments. To this end, we recall that we can rewrite the GPDs as

$$H(x,\xi,t) = H_D(x,\xi,t) + \text{sign}(\xi)\left[D^{\text{Int}}\left(\frac{x}{\xi},t\right) + D^{\text{Ext}}\left(\frac{x}{\xi},t\right)\right], \tag{45}$$

where we have restored the explicit reference to the t dependence. $H_D(x,\xi,t)$ denotes the GPD, yielding the A generalized form factors in Eq. (8), while the D-terms generate the C ones. We highlight the fact that D^{Int} is the intrinsic contribution to the D-term—i.e., that generated by the DD, $G(\beta,\alpha,t) = -\alpha h_P(\beta,\alpha,t)$ [see Eq. (19)]—while D^{Ext} is added as allowed [32,106] and tuned so that the soft-pion theorem is fulfilled.

Then, we compute first-order Mellin moments of GPDs. Following Eq. (8), it reads

$$\int_{-1}^{1} \mathrm{d}x x H_\pi^q(x,\xi,t) = A_{2,0}^q(t) + 4\xi^2 C_2^q(t), \tag{46}$$

where $A_{2,0}^q(t)$ can again be obtained from $\xi \to 0$ limit GPDs, and therefore presents no special difficulty. The result yielded by our two models is shown in the left panel of Fig. 7, together with the most recent experimental extraction [43]. There, a faster decay with the momentum transfer (with respect to experimental data) is observed in both cases, meaning that the expected $1/|t|$ behavior might be violated due to missing contributions in the BSA (see Sec. III B), marking a significant difference from the EFF.

On the contrary, C_2^q is purely generated from the first-order Mellin moment of the sum between the intrinsic and extrinsic D-terms [Eq. (45)]. The soft-pion theorem provides an unambiguous way to fix D^{Ext} at $t = 0$, but as discussed before, its t dependence is left unconstrained.

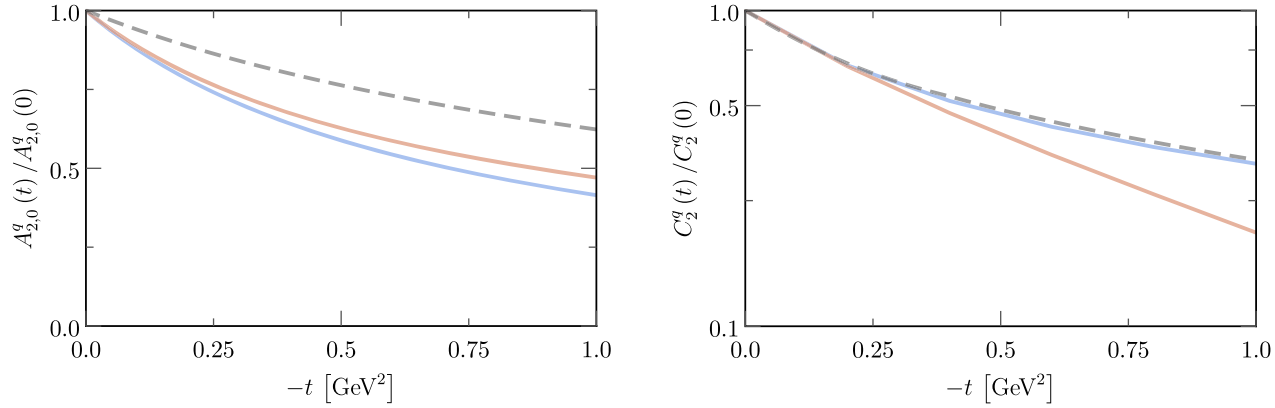

FIG. 7. *Left panel:* Unit-normalized results for the gravitational form factor $A_{2,0}^q(-t)$ computed through the algebraic (blue line) and numerical models (brown line). *Right panel:* Logarithmic scale plot of the unit-normalized gravitational form factor $C_2^q(-t)$ computed through the algebraic (blue line) and numerical models (brown line). The dashed gray line represents the latest extractions from $\gamma^*\gamma \to \pi^0\pi^0$ experimental data [43].

It therefore requires an additional modeling assumption. We decide here to describe it as a monopole [see Eq. (42)]. We assume the mass scale therein to be that in the LFWF, which we fixed through the pion's electromagnetic charge radius (as discussed above). Neither this choice of a monopole-like parametrization nor the existence of one single mass scale relies on first-principles arguments (at least, when working outside Polyakov-Weiss' DDs scheme). However, this simple approach revealed in Fig. 7 (right panel) at low $|t|$ (below 0.5–0.6 GeV^2) shows consistent behavior between the two GPD models on the one hand, and between them and existing extractions for such GFFs [43] on the other hand. This is indeed a crucial requirement for these GPD models, which, apart from fulfilling all the requirements imposed by QCD, are intended to be exploited in the assessment of DVCS (see Sec. VI).

DVCS can be described in terms of GPDs in the low-$|t|$ regime [120,121]. Therefore, the GPD's behavior within that region deserves special attention. In this respect, the "pressure radius" allows for a fair quantification of our accuracy at small momentum transfer. In fact, $r_\pi^{\theta_1}$ can be defined analogously to Eq. (44) [38,39], yielding for our two models

$$\left.\frac{r_\pi^{\theta_1}}{r_\pi}\right|_{\text{Alg.}} = 1.17, \qquad \left.\frac{r_\pi^{\theta_1}}{r_\pi}\right|_{\text{Ding}} = 1.07. \tag{47}$$

These results are in agreement with those extracted from $\gamma^*\gamma \to \pi^0\pi^0$ [43]. Despite the existing model dependence and the simple choice for the D-term's momentum transfer dependence, Eq. (42), the slope at $t \to 0$ of the pressure distribution matches the expectation, even when fixed through an independent quantity (r_π), and thus supports the choice of a monopole-like *Ansatz* for the D-term when the region of interest is that of low t.

Summarizing this section, we obtained GPD models which are unambiguously defined, matching both theoretical and phenomenological expectations, and their suitability for phenomenological analyses becomes manifest.

V. PHENOMENOLOGICAL MODELING

In order to get a comparison at the level of CFFs, since until now no GPD related experimental data are available, we introduce a "phenomenology-like" model based on the Radyushkin double distribution *Ansatz* [44], the xFitter pion PDF set [14], and the t dependence suggested in Ref. [121]. In brief, we model the quark and gluon GPDs as

$$H_\pi^q(x,\xi,t) = \int \mathrm{d}\Omega q_\pi(\beta) h(\beta,\alpha) r(\beta,t) + \frac{\xi}{|\xi|} D^q\left(\frac{x}{\xi},t\right), \tag{48}$$

$$H_\pi^g(x,\xi,t) = \int \mathrm{d}\Omega \beta g_\pi(\beta) h(\beta,\alpha) r(\beta,t) + |\xi| D^g\left(\frac{x}{\xi},t\right), \tag{49}$$

where $\mathrm{d}\Omega = \mathrm{d}\beta\mathrm{d}\alpha\delta(x-\beta-\alpha\xi)\theta(1-|\beta|-|\alpha|)$. The PDFs are given by

$$xq_v(x) = \frac{1}{2} A_v x^{B_v}(1-x)^{C_v}, \tag{50}$$

$$xq_s(x) = \frac{1}{6}\frac{A_S}{\mathcal{B}(B_s+1,C_s+1)} x^{B_s}(1-x)^{C_s}, \tag{51}$$

$$u_\pi(x) = -\theta(-x) q_s(|x|) + \theta(x)(q_v(x)+q_s(x)), \tag{52}$$

$$d_\pi(x) = -\theta(-x)(q_v(|x|)+q_s(|x|)) + \theta(x) q_s(x), \tag{53}$$

$$s_\pi(x) = -\theta(-x) q_s(|x|) + \theta(x) q_s(x), \tag{54}$$

$$xg_\pi(x) = A_g(C_g+1)(1-x)^{C_g}, \tag{55}$$

where $\mathcal{B}$ is the Euler beta function, and the parameters A_i, B_i, and C_i are taken as the central values of the xFitter fit obtained in Ref. [14]. For completeness, they are recalled in Table I. The profile function $h(\beta,\alpha)$ is given by the RDDA:

$$h(\beta,\alpha) = \frac{\Gamma(2N+2)}{2^{2N+1}\Gamma^2(N+1)} \frac{((1-|\beta|)^2-\alpha^2)^N}{(1-|\beta|)^{2N+1}}, \tag{56}$$

where we choose $N=2$. The $r(\beta,t)$ function is then chosen following Refs. [121,122]—i.e., based on Regge phenomenology:

$$r(\beta,t) = \exp\left(t f(|\beta|)\right),$$
$$f(\beta) = (1-\beta)^3\left(\kappa \ln\left(\frac{1}{\beta}\right) + B\right) + A\beta(1-\beta)^2, \tag{57}$$

where $\kappa = 0.9$ GeV^{-2}, with A and B being fitted to the values of the EFF. We obtained $A = 1.48$ GeV^{-2} and $B = 1.14$ GeV^{-2}—i.e., the same order of magnitude as the authors of Ref. [121]. We make the rough assumption that these parameters are the *same* for both quarks and gluons, since the absence of gluon-sensitive data precludes any sensible fit. Finally, just like before, one is left with determining the values of the D-terms $D^q(\alpha)$ and $D^g(\alpha)$,

TABLE I. Parameters for pion PDFs obtained in Ref. [14].

	A_i	B_i	C_i
$i=v$	2.60	0.75	0.95
$i=s$	0.21	0.5	8
$i=g$	0.23	✗	3

this time for both quarks and gluons. Once more, we apply the soft-pion theorem, enforcing that

$$H^q(-x,1,0) = H^q(x,1,0), \qquad H^g(x,1,0) = 0. \quad (58)$$

We therefore define

$$D_0^q(x) = D^q(x,0) = \frac{H^q(-x,1,0) - H^q(x,1,0)}{2}, \quad (59)$$

$$D_0^g(x) = D^g(x,0) = -H^g(x,1,0). \quad (60)$$

Finally, the t dependence of the quark D-term is fitted to the gravitational form factors [43] through the *Ansatz*:

$$D^q(z,t) = \frac{D_0^q(z)}{1 - \frac{t}{\Lambda_{D^q}^2}}, \quad (61)$$

and we find $\Lambda_{D^q}^2 = 0.53\ \text{GeV}^2$. We apply the same *Ansatz* for the gluon and once again, since there are no data available for the latter, we assume $\Lambda_{D^g}^2 = \Lambda_{D^q}^2$. Figure 8 shows the typical results obtained for these GPDs.

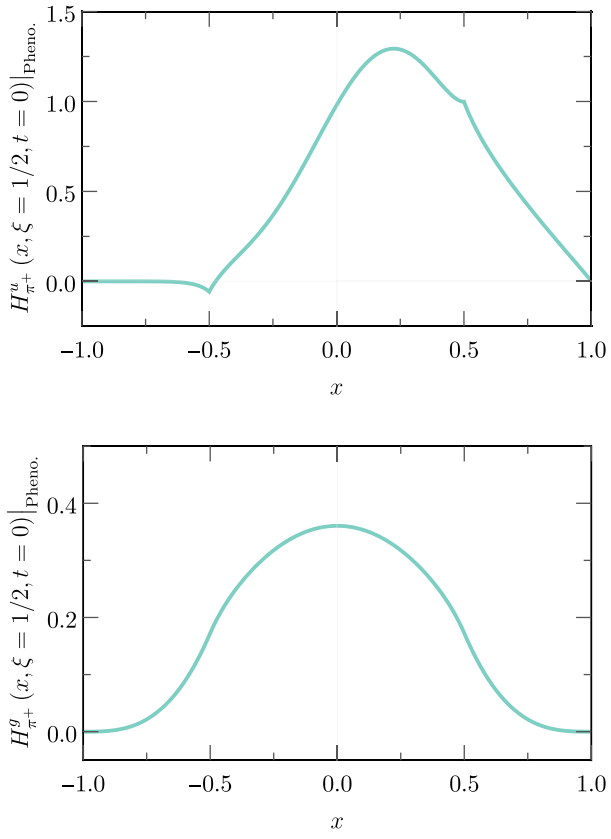

FIG. 8. *Upper panel:* Phenomenological quark GPD model taken at $\xi = 1/2$ and $t = 0$. *Lower panel:* Phenomenological gluon GPD evaluated at $\xi = 1/2$ and $t = 0$. Both shown at the original scale of $\mu^2 = 1.9\ \text{GeV}^2$.

The continuous albeit nondifferentiable property of the GPD at $|x| = |\xi|$ is again manifest on the figure for quarks, and harder to see but present for gluons. We conclude this section by saying that the xFitter Collaboration provides uncertainty bands on the PDF parameters. However, we do not propagate them, as we are interested in a comparison in terms of orders of magnitude, and not in a precise assessment of the compatibility between the phenomenological and numerical models.

VI. FROM GPDS TO COMPTON FORM FACTORS

Now, we would like to assess how the differences between the three models translate into experimental observables that may be reachable through, e.g., the Sullivan process [121]. It should be noted that we have not taken into account virtuality effects here, which can be handled in the CSM framework [123].

A. Evolution

Evolution equations play a markedly different role, whether we are considering the algebraic and numerical models of Sec. III on the one hand, or the phenomenological one given in the previous section on the other hand. Indeed, the latter is defined at a medium scale ($\mu^2_{\text{Ref.}} = 1.9\ \text{GeV}^2$) and is already supplemented with strange quark and gluon distributions. On the contrary, the CSM models are defined at a low scale (i.e., below $1\ \text{GeV}^2$), where effective quarks are expected to be the relevant degrees of freedom to describe the pion. Strange quark and gluon distributions are then purely generated by evolution.

In order to be able to perform the evolution from a low enough scale, we follow the path highlighted in Refs. [34,124]. Namely, we use an effective coupling obtained from lattice-QCD and CSM analyses, which has the interesting property of not presenting a Landau pole and instead saturates in the infrared regime [124–126]. It has been shown that quark and gluon PDFs obtained through that procedure [34,35] are consistent with pion's gluon PDFs computed on the lattice [36,127]. To do that, we employed the PARTONS software [128] in combination with the APFEL++ evolution software [63,129,130]. As an illustration of such a procedure, Fig. 9 shows our three models at a scale of $\mu^2 = 2\ \text{GeV}^2$. Notably, even if it stays null at $\xi = 1$ in agreement with the soft-pion theorem, one can note that evolution provides a significant gluon contribution already for $\xi = 1/2$, in agreement with Ref. [65]. In fact, at $2\ \text{GeV}^2$, the generated gluon distributions are much larger than the one obtained from the phenomenological xFitter/RDDA model. This can be explained by the small-x behavior of the respective PDFs. The xFitter Collaboration has assumed that the gluon PDF behaves like $1/x$ at $\mu^2 = 1.9\ \text{GeV}^2$, while the lattice and CSM gluon PDFs behave at the same scale like $x^{-3/2}$.

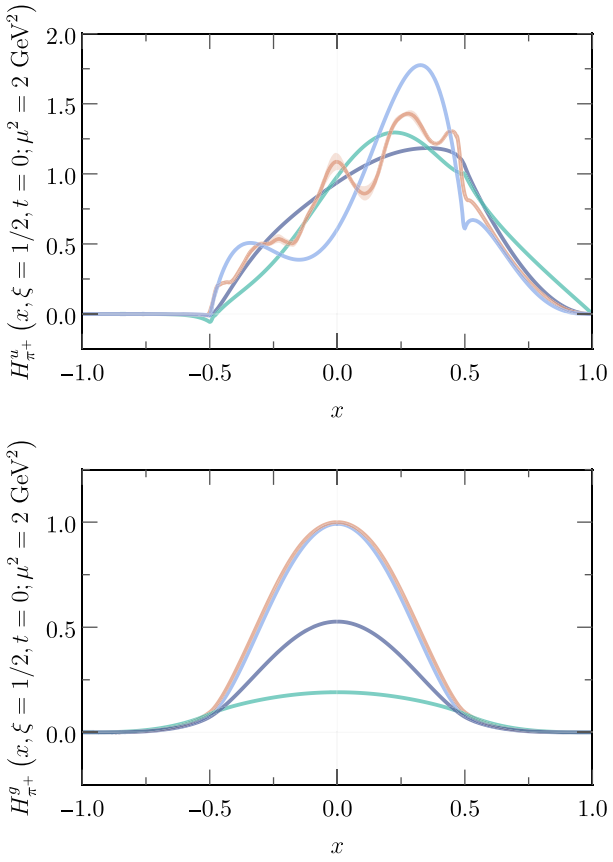

FIG. 9. *Upper panel:* Comparison at $\mu^2 = 2\ \mathrm{GeV}^2$ of the three u-quark GPD models presented in this work at $t = 0$ and $\xi = 1/2$. *Lower panel:* The same thing for gluon GPDs. *Legend:* Algebraic model (blue line), numerical model (brown line), and phenomenological model (green line). The dark blue line represents a fourth model, built according to the strategy of Sec. V but starting from the CSM PDF [34] defined at 1 GeV and added to illustrate the impact of the gluon PDF and evolution in the ERBL region.

Our treatment carries systematic uncertainties that are hard to assess. Nonetheless, it is a direct off-forward extension of the one applied on PDFs [34,124]. The procedure yields, in the forward case, a strong enhancement of the gluon PDF with respect to the xFitter extraction. This enhancement was latter confirmed by lattice-QCD studies of the gluon PDF at 2 GeV [36,127]. This situation highlights our lack of knowledge of the gluon content of the pion, as available experimental data sensitivity to gluons is limited. Forthcoming facilities such as the EIC will therefore be more than welcome. The situation is naturally extended to the off-forward region, where our methodology provides gluon GPDs enhanced with respect to the standard phenomenological model based on xFitter PDFs, illustrating again our ignorance of the gluon content of the pion.

Our CSM-based GPD models come with their uncertainty band, generated by the inversion of the Radon transform. Such uncertainty bands need to be propagated through the evolution. This is particularly relevant for the case of the numerical model. We assess this effect through the replica method: from the uncertainties estimated in Sec. IV A 4, we introduce Gaussian noise at the level of the corresponding DD and generate a set of 250 GPDs at the reference scale. Then, we employ APFEL++ to evolve them up to $\mu^2 = 2\ \mathrm{GeV}^2$. Thus, we are able to generate a band estimating the uncertainties generated through the inverse Radon transform strategy and propagate it by evolution (Fig. 9). We note that the evolution procedure tends to reduce the size of the uncertainty band, stabilizing the results at moderate and high scales.

B. Compton form factors

Using our evolved GPD models, we compute the CFFs entering the description of DVCS using the formulas available in Refs. [131,132] and implemented in the PARTONS framework [128]. The results for the valence region are exhibited in Fig. 10. Interestingly, the imaginary part of the CFF does not seem to be very sensitive to the

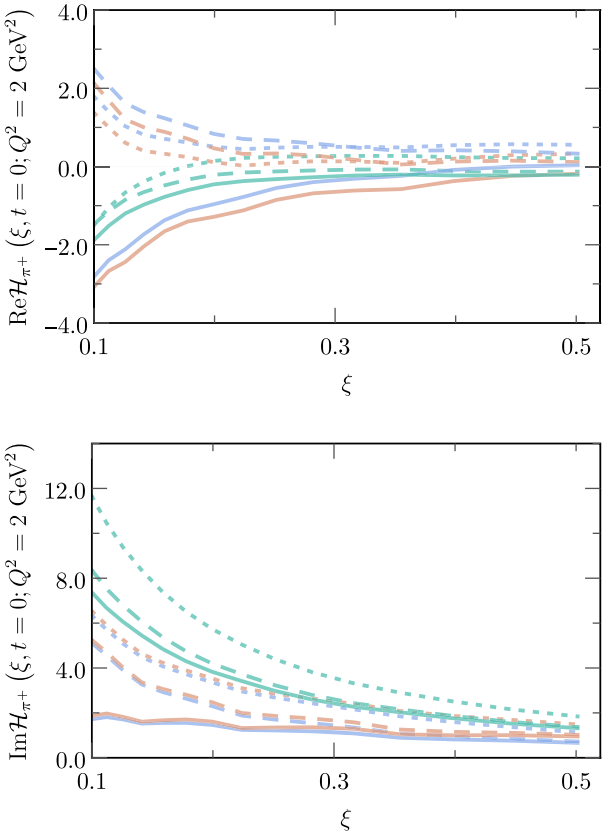

FIG. 10. DVCS Compton form factors within the valence region—i.e., $\xi \in [0.1, 0.5]$. *Upper panel:* Real part. *Lower panel:* Imaginary part. *Legend:* Algebraic model (blue line), numerical model (brown line), and phenomenological model (green line). The dotted line is the LO evaluation, the dashed line is the NLO without the gluon GPDs (see text), and the solid line is the full NLO result.

differences between the algebraic and the numerical models in any of the scenarios considered. The real part presents a sensitivity, but the latter remains small. More precisely, the richer physical content taken into account in the numerical model (including dynamical chiral symmetry breaking) merely generates a 10% difference on the real part of the CFF, and almost nothing on the imaginary one. Therefore, even in the valence region, DVCS seems to be poorly sensitive to the fine modeling assumptions, in agreement with Ref. [11]. And in fact, from the study of the deconvolution of DVCS, one expects the latter to be poorly sensitive to oscillations, explaining why, despite having a large and waving ERBL region for ξ belonging to the valence region (see Fig. 9), the real and imaginary parts of the CFF remain quite smooth. On the other hand, there is a clear difference between the phenomenological model on one side, and the Bethe-Salpeter-derived ones on the other. This is an important outcome, as such a region could be probed by the EicC project, allowing one to discriminate between the two types of model presented here. Although both models fulfill the polynomiality property by construction through a Radon transform, they differ in their large-x behavior: CSM models agree with the pQCD expectation [93,94], while the model introduced in Sec. V does not. Anyhow, the impact of large-x behavior on the CFFs is strongly imbricated with evolution and is therefore hard to estimate. It is not clear that it has a significant impact in the kinematic region we explore in this work.

An additional comment that can be made on Fig. 10 is the key role of gluon GPDs, even in the valence region, thanks to the comparison done at NLO with and without taking them into account. For every model, gluons interfere with quarks, strongly reducing the imaginary part of the CFF when Q^2 remains low (a few GeV^2). The impact is more remarkable on the CSM-based model than on the phenomenological one, but the trend is the same. More dramatically, they also trigger a sign change in the real part of the amplitude for CSM-based models, and they amplify the phenomenon in the case of the phenomenological model.

Outside of the valence region, the picture is modified as displayed in Fig. 11. This time, CSM-based models clearly yield a much larger CFF than the phenomenological one. This can be explained by the differences in the small-x_B behavior of the two types of models, as mentioned previously. Indeed, the ratio between the CSM gluon PDF and the xFitter one behaves like $1/\sqrt{x_B} \simeq 30$ for $x = 10^{-3}$, explaining, at least in terms of orders of magnitude, the differences between the NLO results on the real part of the CFF, and the LO result on the imaginary part (through evolution in this case), as highlighted in Fig. 11. Understanding the other cases (LO computation of the real part, and NLO computation of the imaginary one) is more involved, as the sign differs from one model to the other, highlighting the entangled model dependence.

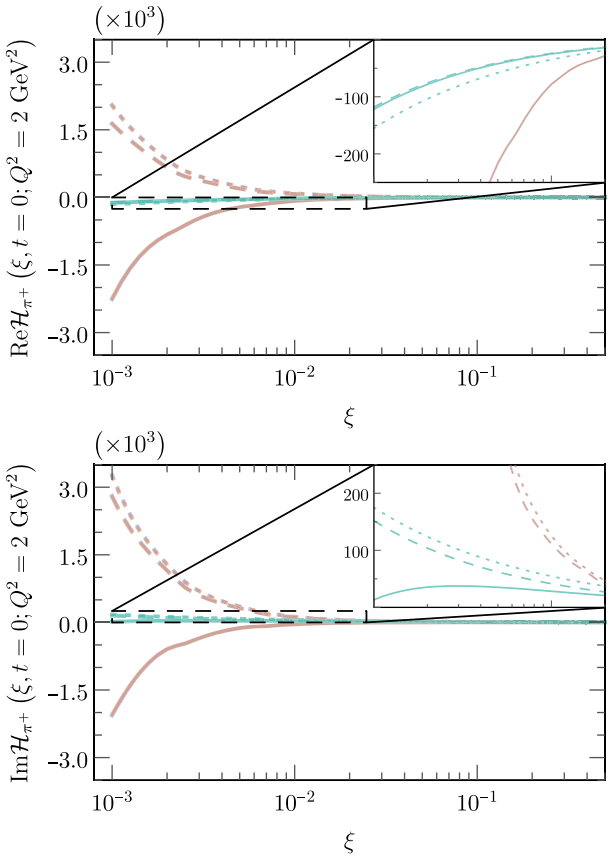

FIG. 11. DVCS Compton form factors. *Upper panel:* Real part. *Lower panel:* Imaginary part. *Legend:* Numerical model (brown line) and phenomenological model (green line). The dotted line is the LO evaluation, the dashed line is the NLO without the gluon GPDs (see text), and the solid line is the full NLO result. The algebraic model yields results essentially indistinguishable from those of the numerical model.

In the low-ξ region (or equivalently, the low-x_B region), the dominance of the gluon is even more obvious, as this time even the sign of the imaginary part of the RDDA-model's CFF is changed. At such low ξ, the differences between the algebraic and numerical CSM models become irrelevant, as evolution together with the convolution of the perturbative kernel washes out the differences. This is again in agreement with the finding of Ref. [11] on the DVCS deconvolution problem.

We note that gluon dominance at low ξ yields a CFF, roughly behaving as $1/\xi^b$ with $b \approx 1.4$ in the case of the numerical model. Such behavior remains compatible with DVCS dispersion relations with one subtracted constant [133]. However, we highlight that our study is a pure NLO one with no small-ξ resummation being taken into account. The latter may have an important impact on the ξ behavior of the CFF in the low-ξ region. We leave this point for a future work.

Finally, we would like to stress an interesting feature of the present study—namely, that due to gluon GPDs, the real and imaginary parts of the CFF change sign at given values ξ_0, which run with Q^2. This is illustrated in Fig. 11, where we see that NLO corrections without taking gluon GPDs into account keep the same sign as the LO results. Only the inclusion of gluon GPDs triggers a zero crossing in the real and imaginary parts of the CFF. The Q^2 dependence can be understood in the following way: if at some scale Q_1^2 and at some skewness ξ_1 the imaginary part of the CFF is dominated by gluons (i.e., it is negative), increasing the scale should reduce the impact of NLO corrections. Therefore, one expects that at some sufficiently high scale Q_2^2, the CFF evaluated at ξ_1 will turn positive. In other words, the zero crossing is shifted toward lower values of ξ when Q^2 increases. This is precisely what we observe, as displayed in Fig. 12. Interestingly, our phenomenological model undergoes such a zero crossing over the entire Q^2 range studied here. On the other hand, the two CSM-based models exhibit an abrupt step at $Q^2 \simeq 10$–20 GeV^2, for both the real and imaginary parts of the CFF. We also note that, contrary to other features of CFFs, the zero crossing in the real part of the latter allows one to clearly differentiate between the algebraic and numerical models. This might be an experimental signal able to distinguish between the different physical assumptions used. However, the real part of the CFF is usually more difficult to extract experimentally, and thus the study of the consequences of this zero crossing on the DVCS cross section and asymmetries is left for a future work.

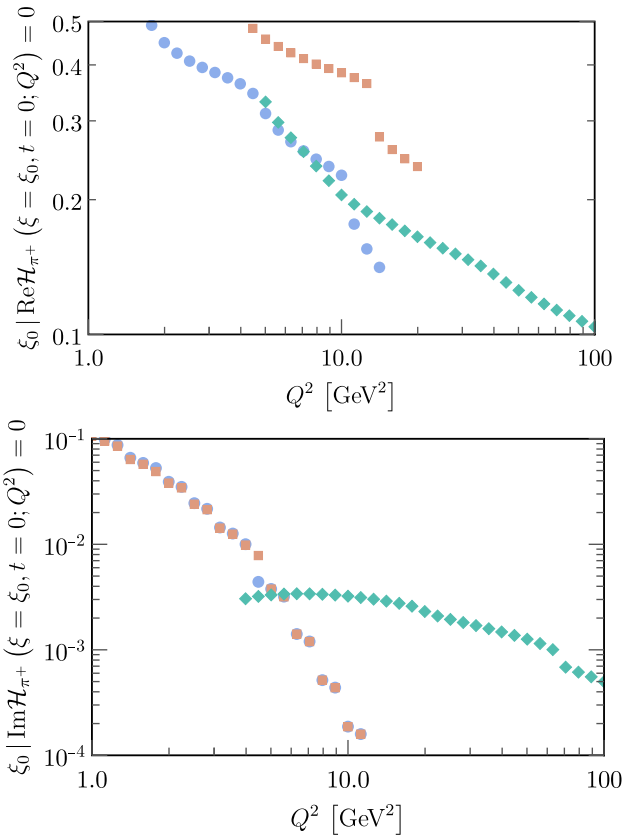

FIG. 12. *Upper panel:* Q^2 displacement of $\xi_0|\mathrm{Re}\mathcal{H}_{\pi^+}(\xi_0, t=0; Q^2)=0$. *Lower panel:* Q^2 displacement of $\xi_0|\mathrm{Im}\mathcal{H}_{\pi^+}(\xi_0, t=0; Q^2)=0$. *Legend:* Algebraic model (blue dots), numerical model (brown squares), and phenomenological model (green rhombuses). As Q^2 increases, ξ_0 decreases, pushing the gluon dominance toward lower values of x_B, as we would naively expect from a perturbative expansion.

VII. CONCLUSION

As we illustrated, the path to building GPD models able to fulfill by construction all the theoretical constraints that apply to these matrix elements is tough. Nevertheless, we showed a way to go, taking advantage of *ab initio* computations of the Bethe-Salpeter wave function of the pion. Combining the mathematical structure of the overlap of LFWFs together with the properties of the inverse Radon transform, we built a pion-quark GPD able to fulfill by construction all the required theoretical properties. We also take the opportunity to improve the numerical solution presented previously in Refs. [32,33], allowing us to assess the numerical uncertainties triggered by the ill-conditioned character of the inverse Radon transform, and highlight the filtering character of the evolution kernel. This allowed us to build for the first time a consistent GPD from a numerical solution of the Bethe-Salpeter equation, something which was long sought (see, for instance, Refs. [29–31,134,135]).

Our work also validates PARTONS [128] as a modular tool able to bridge the gap between nonperturbative QCD practitioners, using either continuum or lattice techniques, and physical observables related to the 3D structure of hadrons. We stress once again the crucial role played by evolution in this study that we exploited through the APFEL++ library [129,130]. Its combined usage with PARTONS made it possible to compute CFFs on a large range of ξ, t, and Q^2 kinematical points covering the kinematical regions explored at both EIC and EicC. This has revealed two interesting features: (i) the remarkable sign change in the imaginary part of the CFF, testifying of the importance of the gluon GPD, and (ii) a feasibility study of accessing experimentally pion GPDs at EIC and EicC using the Sullivan process [120] (see also Refs. [41,42,123]), something advocated in the EIC Yellow Report [136]. This study is presented in a dedicated paper [137].

Finally, we mention that our study on the pion has consequences at the level of the nucleon. Indeed, the validation of the computing chain for the pion holds for the nucleon, highlighting the fact that PARTONS is ready for phenomenological studies of DVCS at NLO. On top of this, the physical behavior of the CFF, especially the sign change of the imaginary part, might well be something that will be observed also for the nucleon. Further study in that

direction must be performed before the EIC can start accumulating data.

ACKNOWLEDGMENTS

We are grateful to Qin-Tao Song for kindly providing us the GFF data obtained from pion GDA. We would like to thank P. Barry, H. Dutrieux, T. Meisgny, B. Pire, K. Raya, C. D. Roberts, P. Sznajder, and J. Wagner for interesting discussions and stimulating comments. This work is supported by the University of Huelva under Grant No. EPIT-2020 (J. M. M. C.). F. S., J. R. Q., and J. S. acknowledge support from Ministerio de Ciencia e Innovación (Spain) under Grant No. PID2019–107844 GB-C22; Junta de Andaluca, under the 2014–2020 FEDER Contracts No. UHU-1264517, No. P18-1321FR-5057 and PAIDI FQM-370. This project was supported by the European Union's Horizon 2020 research and innovation program under Grant Agreement No. 824093. This work is supported in part in the framework of the GLUODYNAMICS project funded by the "P2IO LabEx (ANR-10-LABX-0038)" in the framework "Investissements d'Avenir" (ANR-11-IDEX-0003-01) managed by the Agence Nationale de la Recherche (ANR), France.

APPENDIX: INVERTIBILITY OF $\mathcal{R}^T\mathcal{R}$

In Sec. IV, we addressed the problem of computing DDs by solving a squared linear system whose matrix is written as

$$(\mathcal{R}^T\mathcal{R})_{jk} = \sum_i R_{ij}R_{ik}, \tag{A1}$$

where $\mathcal{R}_{ij}$ is the contribution of the element j to the integral over the line $x_i - \beta - \alpha\xi_i = 0$ with (x_i, ξ_i) in the DGLAP region. Its inversion is a necessary step for the solution of the inverse Radon transform problem. Thus, the condition of maximal rank for the matrix $\mathcal{R}^T\mathcal{R}$ must be fulfilled.

As we shall prove through this Appendix, such a condition is unavoidably met if the Radon transform matrix, $\mathcal{R}$, has maximal rank—a condition which, as discussed in Sec. IV A 2, can be assumed to be true without loss of generality.

Prior to our proof for the invertibility of $\mathcal{R}^T\mathcal{R}$, we must present the two central pieces of our arguments:

1. Rank-nullity theorem:

Let V, W be finite-dimensional $\mathbb{F}$-vector spaces and $T: V \to W$ a linear application. Then, the *rank-nullity theorem* states

$$\begin{aligned}\dim_{\mathbb{F}} V &= \dim_{\mathbf{F}} T(V) + \dim_{\mathbf{F}} \ker(T) \\ &= \mathrm{Rank}(T) + \dim \mathcal{N}(T),\end{aligned} \tag{A2}$$

with $\mathcal{N}(T)$ denoting the null space of the application.

In particular, for a matrix $\mathcal{A} \in \mathcal{M}_{m,n}(k)$, with $m \geq n$:

$$n = \mathrm{Rank}(\mathcal{A}) + \dim \mathcal{N}(\mathcal{A}), \tag{A3}$$

from which one can straightforwardly deduce that

$$\dim \mathcal{N}(A) = 0 \Leftrightarrow \mathrm{Rank}(\mathcal{A}) = n, \tag{A4}$$

i.e., the matrix $\mathcal{A}$ has maximal rank.

Therefore, in the particular situation where the matrix $\mathcal{A}_n$ is squared—i.e., $m = n$—the condition $\dim \mathcal{N}(\mathcal{A}_n) = 0$ implies that such a matrix has maximal rank, and thus, by means of the *Rouché-Frobenius theorem*, that such a matrix is invertible:

$$\dim \mathcal{N}(\mathcal{A}_n) = 0 \Leftrightarrow \exists\, \mathcal{A}_n^{-1} \in \mathcal{M}_n | \mathcal{A}_m \mathcal{A}_n^{-1} = \mathcal{A}_n^{-1}\mathcal{A} = \mathbb{I}_n. \tag{A5}$$

2. $\mathcal{N}(A) = \mathcal{N}(\mathcal{A}^T\mathcal{A})$:

Once again, let us consider an arbitrary matrix $\mathcal{A} \in \mathcal{M}_{m,n}(k)$, with $m \geq n$ and a vector $x \in \mathcal{N}(A)$. Applying $\mathcal{A}^T\mathcal{A} \in \mathcal{M}_n(k)$ on it,

$$\mathcal{A}^T\mathcal{A}x = \mathcal{A}^T\mathbf{0} = \mathbf{0}, \tag{A6}$$

where the first identity follows from the definition of $\mathcal{N}(\mathcal{A})$, it immediately implies that $x \in \mathcal{N}(\mathcal{A}^T\mathcal{A}) \Rightarrow \mathcal{N}(A) \subset \mathcal{N}(\mathcal{A}^T\mathcal{A})$.

Equivalently, consider a vector $x \in \mathcal{N}(\mathcal{A}^T\mathcal{A})$. Then,

$$(\mathcal{A}^T\mathcal{A})x = \mathbf{0} \Rightarrow x^T(\mathcal{A}^T\mathcal{A})x = x^T\mathbf{0} = \mathbf{0}, \tag{A7}$$

and thus,

$$x^T(\mathcal{A}^T\mathcal{A})x = (\mathcal{A}x)^T(\mathcal{A}x) = ||\mathcal{A}x||^2 = 0, \tag{A8}$$

where $||\cdot||$ denotes the vector norm.

Because $\mathcal{A}$ is different from the null operator, it follows that

$$||\mathcal{A}x||^2 = 0 \Rightarrow \mathcal{A}x = \mathbf{0}; \tag{A9}$$

thus, $x \in \mathcal{N}(A) \Rightarrow \mathcal{N}(\mathcal{A}^T\mathcal{A}) \subset \mathcal{N}(\mathcal{A})$.

The combination of these two results implies

$$\mathcal{N}(A) = \mathcal{N}(\mathcal{A}^T\mathcal{A}). \tag{A10}$$

Keeping this in mind lets us turn to the specific problem we are involved with. Consider $\mathcal{R} \in \mathcal{M}_{m\times n}(\mathbb{R})$, the Radon transform matrix of Sec. IV, with $m \geq n$. And the matrix $\mathcal{R}^T\mathcal{R} \in \mathcal{M}_n(\mathbb{R})$, where $\mathcal{R}^T$ stands for the transposed Radon transform matrix.

By hypothesis, $\mathrm{Rank}\,(\mathcal{R}) = n$, as discussed in Sec. IV A 2. Therefore, by means of Eq. (A4), $\dim\mathcal{N}(\mathcal{R}) = 0$. Furthermore, relation (A10) guarantees that $\dim\mathcal{N}(\mathcal{R}^T\mathcal{R}) = \dim\mathcal{N}(\mathcal{R}) = 0$. Then, through Eq. (A5), the matrix $(\mathcal{R}^T\mathcal{R})^{-1}$ exists.

[1] D. Müeller, D. Robaschik, B. Geyer, F. M. Dittes, and J. Hořejši, Wave functions, evolution equations and evolution kernels from light ray operators of QCD, Fortschr. Phys. **42**, 101 (1994).

[2] X. Ji, Deeply virtual Compton scattering, Phys. Rev. D **55**, 7114 (1997).

[3] X. Ji, Gauge-Invariant Decomposition of Nucleon Spin, Phys. Rev. Lett. **78**, 610 (1997).

[4] A. V. Radyushkin, Asymmetric gluon distributions and hard diffractive electroproduction, Phys. Lett. B **385**, 333 (1996).

[5] A. V. Radyushkin, Nonforward parton distributions, Phys. Rev. D **56**, 5524 (1997).

[6] M. Diehl, Generalized parton distributions, Phys. Rep. **388**, 41 (2003).

[7] A. V. Belitsky and A. V. Radyushkin, Unraveling hadron structure with generalized parton distributions, Phys. Rep. **418**, 1 (2005).

[8] K. Kumericki, S. Liuti, and H. Moutarde, GPD phenomenology and DVCS fitting, Eur. Phys. J. A **52**, 157 (2016).

[9] M. Burkardt, Impact parameter dependent parton distributions and off forward parton distributions for $\zeta \to 0$, Phys. Rev. D **62**, 071503 (2000); Erratum, Phys. Rev. D **66**, 119903 (2002).

[10] M. V. Polyakov, Generalized parton distributions and strong forces inside nucleons and nuclei, Phys. Lett. B **555**, 57 (2003).

[11] V. Bertone, H. Dutrieux, C. Mezrag, H. Moutarde, and P. Sznajder, Deconvolution problem of deeply virtual Compton scattering, Phys. Rev. D **103**, 114019 (2021).

[12] V. Bertone, H. Dutrieux, C. Mezrag, H. Moutarde, and P. Sznajder, Shadow generalized parton distributions: A practical approach to the deconvolution problem of DVCS, in *28th International Workshop on Deep Inelastic Scattering and Related Subjects* (2021).

[13] P. C. Barry, N. Sato, W. Melnitchouk, and C.-R. Ji, First Monte Carlo Global QCD Analysis of Pion Parton Distributions, Phys. Rev. Lett. **121**, 152001 (2018).

[14] I. Novikov *et al.*, Parton distribution functions of the charged pion within the xFitter framework, Phys. Rev. D **102**, 014040 (2020).

[15] C. Han, G. Xie, R. Wang, and X. Chen, An analysis of parton distribution functions of the pion and the kaon with the maximum entropy input, Eur. Phys. J. C **81**, 302 (2021).

[16] P. C. Barry, C.-R. Ji, N. Sato, and W. Melnitchouk, Global QCD Analysis of Pion Parton Distributions with Threshold Resummation, Phys. Rev. Lett. **127**, 232001 (2021).

[17] X. Ji, Parton Physics on a Euclidean Lattice, Phys. Rev. Lett. **110**, 262002 (2013).

[18] Y.-Q. Ma and J.-W. Qiu, Extracting parton distribution functions from lattice QCD calculations, Phys. Rev. D **98**, 074021 (2018).

[19] A. V. Radyushkin, Quasi-parton distribution functions, momentum distributions, and pseudo-parton distribution functions, Phys. Rev. D **96**, 034025 (2017).

[20] A. J. Chambers, R. Horsley, Y. Nakamura, H. Perlt, P. E. L. Rakow, G. Schierholz, A. Schiller, K. Somfleth, R. D. Young, and J. M. Zanotti, Nucleon Structure Functions from Operator Product Expansion on the Lattice, Phys. Rev. Lett. **118**, 242001 (2017).

[21] K. Cichy and M. Constantinou, A guide to light-cone PDFs from Lattice QCD: An overview of approaches, techniques and results, Adv. High Energy Phys. **2019**, 3036904 (2019).

[22] B. Joó, J. Karpie, K. Orginos, A. V. Radyushkin, D. G. Richards, R. S. Sufian, and S. Zafeiropoulos, Pion valence structure from Ioffe-time parton pseudodistribution functions, Phys. Rev. D **100**, 114512 (2019).

[23] M. Constantinou *et al.*, Parton distributions and lattice-QCD calculations: Toward 3D structure, Prog. Part. Nucl. Phys. **121**, 103908 (2021).

[24] X. Gao, L. Jin, C. Kallidonis, N. Karthik, S. Mukherjee, P. Petreczky, C. Shugert, S. Syritsyn, and Y. Zhao, Valence parton distribution of the pion from lattice QCD: Approaching the continuum limit, Phys. Rev. D **102**, 094513 (2020).

[25] J.-W. Chen, H.-W. Lin, and J.-H. Zhang, Pion generalized parton distribution from lattice QCD, Nucl. Phys. **B952**, 114940 (2020).

[26] H.-W. Lin, Nucleon Tomography and Generalized Parton Distribution at Physical Pion Mass from Lattice QCD, Phys. Rev. Lett. **127**, 182001 (2021).

[27] C. Alexandrou, K. Cichy, M. Constantinou, K. Hadjiyiannakou, K. Jansen, A. Scapellato, and F. Steffens, Unpolarized and Helicity Generalized Parton Distributions of the Proton within Lattice QCD, Phys. Rev. Lett. **125**, 262001 (2020).

[28] L. Chang, C. Mezrag, H. Moutarde, C. D. Roberts, J. Rodriguez-Quintero, and P. C. Tandy, Basic features of the

pion valence-quark distribution function, Phys. Lett. B **737**, 23 (2014).
[29] C. Mezrag, H. Moutarde, J. Rodríguez-Quintero, and F. Sabatié, Towards a pion generalized parton distribution model from Dyson-Schwinger equations, arXiv: 1406.7425.
[30] C. Mezrag, L. Chang, H. Moutarde, C. D. Roberts, J. Rodríguez-Quintero, F. Sabatié, and S. M. Schmidt, Sketching the pion's valence-quark generalised parton distribution, Phys. Lett. B **741**, 190 (2015).
[31] C. Mezrag, H. Moutarde, and J. Rodriguez-Quintero, From Bethe-Salpeter wave functions to generalised parton distributions, Few Body Syst. **57**, 729 (2016).
[32] N. Chouika, C. Mezrag, H. Moutarde, and J. Rodríguez-Quintero, Covariant extension of the GPD overlap representation at low Fock states, Eur. Phys. J. C **77**, 906 (2017).
[33] N. Chouika, C. Mezrag, H. Moutarde, and J. Rodríguez-Quintero, A Nakanishi-based model illustrating the covariant extension of the pion GPD overlap representation and its ambiguities, Phys. Lett. B **780**, 287 (2018).
[34] M. Ding, K. Raya, D. Binosi, L. Chang, C. D. Roberts, and S. M. Schmidt, Symmetry, symmetry breaking, and pion parton distributions, Phys. Rev. D **101**, 054014 (2020).
[35] Z.-F. Cui, M. Ding, F. Gao, K. Raya, D. Binosi, L. Chang, C. D. Roberts, J. Rodríguez-Quintero, and S. M. Schmidt, Kaon and pion parton distributions, Eur. Phys. J. C **80**, 1064 (2020).
[36] L. Chang and C. D. Roberts, Regarding the distribution of glue in the pion, Chin. Phys. Lett. **38**, 081101 (2021).
[37] C. Shi, K. Bednar, I. C. Cloët, and A. Freese, Spatial and momentum imaging of the pion and kaon, Phys. Rev. D **101**, 074014 (2020).
[38] K. Raya, Z.-F. Cui, L. Chang, J. M. Morgado, C. D. Roberts, and J. Rodriguez-Quintero, Revealing pion and kaon structure via generalised parton distributions, Chin. Phys. C **46**, 013105 (2022).
[39] J.-L. Zhang, K. Raya, L. Chang, Z.-F. Cui, J. M. Morgado, C. D. Roberts, and J. Rodríguez-Quintero, Measures of pion and kaon structure from generalised parton distributions, Phys. Lett. B **815**, 136158 (2021).
[40] D. Binosi, L. Chang, J. Papavassiliou, S.-X. Qin, and C. D. Roberts, Symmetry preserving truncations of the gap and Bethe-Salpeter equations, Phys. Rev. D **93**, 096010 (2016).
[41] A. C. Aguilar *et al.*, Pion and Kaon structure at the electron-ion collider, Eur. Phys. J. A **55**, 190 (2019).
[42] G. M. Huber *et al.*, Charged pion form-factor between $Q^2 = 0.60$ GeV^2 and 2.45 GeV^2: II. Determination of, and results for, the pion form-factor, Phys. Rev. C **78**, 045203 (2008).
[43] S. Kumano, Q.-T. Song, and O. Teryaev, Hadron tomography by generalized distribution amplitudes in pion-pair production process $\gamma^*\gamma \to \pi^0\pi^0$ and gravitational form factors for pion, Phys. Rev. D **97**, 014020 (2018).
[44] I. V. Musatov and A. V. Radyushkin, Evolution and models for skewed parton distributions, Phys. Rev. D **61**, 074027 (2000).
[45] M. Diehl and T. Gousset, Time ordering in off diagonal parton distributions, Phys. Lett. B **428**, 359 (1998).
[46] M. Diehl, T. Gousset, B. Pire, and O. Teryaev, Probing Partonic Structure in $\gamma^*\gamma \to \pi\pi$ Near Threshold, Phys. Rev. Lett. **81**, 1782 (1998).
[47] M. Diehl, T. Gousset, and B. Pire, Exclusive production of pion pairs in $\gamma^*\gamma$ collisions at large Q^2, Phys. Rev. D **62**, 073014 (2000).
[48] B. Pire, J. Soffer, and O. Teryaev, Positivity constraints for off-forward parton distributions, Eur. Phys. J. C **8**, 103 (1999).
[49] A. V. Radyushkin, Double distributions and evolution equations, Phys. Rev. D **59**, 014030 (1998).
[50] M. Diehl, T. Feldmann, R. Jakob, and P. Kroll, The overlap representation of skewed quark and gluon distributions, Nucl. Phys. **B596**, 33 (2001).
[51] P. V. Pobylitsa, Disentangling positivity constraints for generalized parton distributions, Phys. Rev. D **65**, 114015 (2002).
[52] P. V. Pobylitsa, Positivity bounds on generalized parton distributions in impact parameter representation, Phys. Rev. D **66**, 094002 (2002).
[53] X. Ji, Off forward parton distributions, J. Phys. G **24**, 1181 (1998).
[54] A. V. Radyushkin, Symmetries and structure of skewed and double distributions, Phys. Lett. B **449**, 81 (1999).
[55] M. V. Polyakov and C. Weiss, Skewed and double distributions in pion and nucleon, Phys. Rev. D **60**, 114017 (1999).
[56] F. Yuan, Generalized parton distributions at $x \to 1$, Phys. Rev. D **69**, 051501 (2004).
[57] P. Hoodbhoy, X. Ji, and F. Yuan, Probing Quark Distribution Amplitudes Through Generalized Parton Distributions at Large Momentum Transfer, Phys. Rev. Lett. **92**, 012003 (2004).
[58] G. P. Lepage and S. J. Brodsky, Exclusive processes in perturbative quantum chromodynamics, Phys. Rev. D **22**, 2157 (1980).
[59] A. V. Efremov and A. V. Radyushkin, Factorization and asymptotical behavior of pion form-factor in QCD, Phys. Lett. **94B**, 245 (1980).
[60] B. Melic, B. Nizic, and K. Passek, Complete next-to-leading order perturbative QCD prediction for the pion form-factor, Phys. Rev. D **60**, 074004 (1999).
[61] J. C. Collins and A. Freund, Proof of factorization for deeply virtual Compton scattering in QCD, Phys. Rev. D **59**, 074009 (1999).
[62] X. Ji and J. Osborne, One loop corrections and all order factorization in deeply virtual Compton scattering, Phys. Rev. D **58**, 094018 (1998).
[63] V. Bertone and Collaborators, Revisiting evolution equations for generalised parton distributions (to be published).
[64] M. V. Polyakov, Hard exclusive electroproduction of two pions and their resonances, Nucl. Phys. **B555**, 231 (1999).
[65] W. Broniowski, E. Ruiz Arriola, and K. Golec-Biernat, Generalized parton distributions of the pion in chiral quark models and their QCD evolution, Phys. Rev. D **77**, 034023 (2008).
[66] L. Theussl, S. Noguera, and V. Vento, Generalized parton distributions of the pion in a Bethe-Salpeter approach, Eur. Phys. J. A **20**, 483 (2004).

[67] A. Hertle, Continuity of the Radon transform and its inverse on Euclidean space, Math. Z. **184**, 165 (1983).

[68] O. Teryaev, Crossing and Radon tomography for generalized parton distributions, Phys. Lett. B **510**, 125 (2001).

[69] P. V. Pobylitsa, Solution of polynomiality and positivity constraints on generalized parton distributions, Phys. Rev. D **67**, 034009 (2003).

[70] S. J. Brodsky, H.-C. Pauli, and S. S. Pinsky, Quantum chromodynamics and other field theories on the light cone, Phys. Rep. **301**, 299 (1998).

[71] M. Diehl, Generalized parton distributions in impact parameter space, Eur. Phys. J. C **25**, 223 (2002).

[72] S. J. Brodsky, M. Diehl, and D. S. Hwang, Light cone wave function representation of deeply virtual Compton scattering, Nucl. Phys. **B596**, 99 (2001).

[73] G. Eichmann, H. Sanchis-Alepuz, R. Williams, R. Alkofer, and C. S. Fischer, Baryons as relativistic three-quark bound states, Prog. Part. Nucl. Phys. **91**, 1 (2016).

[74] C. S. Fischer, QCD at finite temperature and chemical potential from Dyson-Schwinger equations, Prog. Part. Nucl. Phys. **105**, 1 (2019).

[75] S.-X. Qin and C. D. Roberts, Resolving the Bethe-Salpeter kernel, Chin. Phys. Lett. **38**, 071201 (2021).

[76] C. Mezrag and G. Salmé, Fermion and photon gap-equations in Minkowski space within the Nakanishi integral representation method, Eur. Phys. J. C **81**, 34 (2021).

[77] S.-S. Xu, L. Chang, C. D. Roberts, and H.-S. Zong, Pion and kaon valence-quark parton quasidistributions, Phys. Rev. D **97**, 094014 (2018).

[78] M. Burkardt, Generalized parton distributions for large x, Phys. Lett. B **595**, 245 (2004).

[79] D. Brommel, M. Diehl, M. Gockeler, Ph. Hagler, R. Horsley, D. Pleiter, P. E. L. Rakow, A. Schafer, G. Schierholz, and J. M. Zanotti, Structure of the pion from full lattice QCD, Proc. Sci., LAT2005 (**2006**) 360.

[80] G. F. de Teramond, T. Liu, R. S. Sufian, H. G. Dosch, S. J. Brodsky, and A. Deur, Universality of Generalized Parton Distributions in Light-Front Holographic QCD, Phys. Rev. Lett. **120**, 182001 (2018).

[81] M. Rinaldi, GPDs at non-zero skewness in ADS/QCD model, Phys. Lett. B **771**, 563 (2017).

[82] J. Lan, C. Mondal, S. Jia, X. Zhao, and J. P. Vary, Pion and kaon parton distribution functions from basis light front quantization and QCD evolution, Phys. Rev. D **101**, 034024 (2020).

[83] E. E. Salpeter and H. A. Bethe, A relativistic equation for bound state problems, Phys. Rev. **84**, 1232 (1951).

[84] M. Gell-Mann and F. Low, Bound states in quantum field theory, Phys. Rev. **84**, 350 (1951).

[85] N. Nakanishi, *Graph Theory and Feynman Integrals* (Gordon and Breach, New York, 1971).

[86] N. Nakanishi, Partial-Wave Bethe-Salpeter equation, Phys. Rev. **130**, 1230 (1963).

[87] N. Nakanishi, A general survey of the theory of the Bethe-Salpeter equation, Prog. Theor. Phys. Suppl. **43**, 1 (1969).

[88] L. Chang, I. C. Cloet, J. J. Cobos-Martinez, C. D. Roberts, S. M. Schmidt, and P. C. Tandy, Imaging Dynamical Chiral Symmetry Breaking: Pion Wave Function on the Light Front, Phys. Rev. Lett. **110**, 132001 (2013).

[89] C. Chen, L. Chang, C. D. Roberts, S. Wan, and H.-S. Zong, Valence-quark distribution functions in the kaon and pion, Phys. Rev. D **93**, 074021 (2016).

[90] G. Salmé, W. de Paula, T. Frederico, and M. Viviani, Two-fermion Bethe-Salpeter equation in Minkowski space: The Nakanishi way, Few Body Syst. **58**, 118 (2017).

[91] J. Carbonell, T. Frederico, and V. A. Karmanov, Bound state equation for the Nakanishi weight function, Phys. Lett. B **769**, 418 (2017).

[92] J. Carbonell, T. Frederico, and V. A. Karmanov, Euclidean to Minkowski Bethe-Salpeter amplitude and observables, Eur. Phys. J. C **77**, 58 (2017).

[93] A. Courtoy and P. M. Nadolsky, Testing momentum dependence of the nonperturbative hadron structure in a global QCD analysis, Phys. Rev. D **103**, 054029 (2021).

[94] Z. F. Cui, M. Ding, J. M. Morgado, K. Raya, D. Binosi, L. Chang, J. Papavassiliou, C. D. Roberts, J. Rodríguez-Quintero, and S. M. Schmidt, Concerning pion parton distributions, Eur. Phys. J. A **58**, 10 (2022).

[95] J. Collins, The non-triviality of the vacuum in light-front quantization: An elementary treatment, arXiv:1801.03960.

[96] D. S. Hwang and D. Müeller, Implication of the overlap representation for modelling generalized parton distributions, Phys. Lett. B **660**, 350 (2008).

[97] D. Müller, Double distributions and generalized parton distributions from the parton number conserved light front wave function overlap representation, arXiv:1711.09932.

[98] B. C. Tiburzi, Double distributions: Loose ends, Phys. Rev. D **70**, 057504 (2004).

[99] J. R. Shewchuk, Triangle: Engineering a 2D quality mesh generator and Delaunay triangulator, edited by M. C. Lin and D. Manocha *Applied Computational Geometry Towards Geometric Engineering* (Springer Berlin Heidelberg, Berlin, Heidelberg, 1996), pp. 203–222.

[100] J. Hadamard, *Sur les problèmes aux dérivées partielles et leur signification physique* (Princeton University Bulletin, Princeton, New Jersey, 1902), pp. 49–52.

[101] V. Maz'ya and T. Shaposhnikova, *Jacques Hadamard: A Universal Mathematician (History of Mathematics)*, Vol. 14 (American Mathematical Society, Providence, RI, 1998).

[102] F. Natterer, *The Mathematics of Computerized Tomography*, Classics in Applied Mathematics (Vieweg+Teubner Verlag, Wiesbaden, 2001).

[103] The condition number of a matrix, $\mathcal{A} \in \mathcal{M}_{m\times n}$, is defined as $\kappa(\mathcal{A}) \coloneqq \sigma_+(\mathcal{A})/\sigma_-(\mathcal{A})$, with $\sigma_\pm(\mathcal{A})$ being the largest and smallest singular values of the matrix $\mathcal{A}$, respectively. A matrix is said to be badly conditioned if $\kappa(\mathcal{A})$ is "large."

[104] D. C.-L. Fong and M. Saunders, LSMR: An iterative algorithm for sparse least-squares problems, SIAM J. Sci. Comput. **33**, 2950 (2011).

[105] W. H. Press, B. P. Flannery, S. A. Teukolsky, W. T. Vetterling *et al.*, *Numerical Recipes* (Cambridge University Press, Cambridge, England, 1989).

[106] D. Mueller and K. M. Semenov-Tian-Shansky, $J = 0$ fixed pole and D-term form factor in deeply virtual Compton scattering, Phys. Rev. D **92**, 074025 (2015).

[107] C. Mezrag, H. Moutarde, and F. Sabatié, Test of two new parameterizations of the generalized parton distribution H, Phys. Rev. D **88**, 014001 (2013).

[108] S. R. Amendolia *et al.*, A measurement of the space-like pion electromagnetic form-factor, Nucl. Phys. **B277**, 168 (1986).

[109] C. N. Brown, C. R. Canizares, W. E. Cooper, A. M. Eisner, G. J. Feldmann, C. A. Lichtenstein, L. Litt, W. Loceretz, V. B. Montana, and F. M. Pipkin, Coincidence electroproduction of charged pions and the pion form-factor, Phys. Rev. D **8**, 92 (1973).

[110] C. J. Bebek *et al.*, Further measurements of forward-charged-pion electroproduction at large k^2, Phys. Rev. D **9**, 1229 (1974).

[111] C. J. Bebek, C. N. Brown, M. Herzlinger, S. D. Holmes, C. A. Lichtenstein, F. M. Pipkin, S. Raither, and L. K. Sisterson, Measurement of the pion form-factor up to $q^2 = 4$ GeV^2, Phys. Rev. D **13**, 25 (1976).

[112] C. J. Bebek *et al.*, Electroproduction of single pions at low epsilon and a measurement of the pion form-factor up to $q^2 = 10$ GeV^2, Phys. Rev. D **17**, 1693 (1978).

[113] E. B. Dally *et al.*, Direct Measurement of the π^- Form-Factor, Phys. Rev. Lett. **39**, 1176 (1977).

[114] P. Brauel, T. Canzler, D. Cords, R. Felst, G. Grindhammer, M. Helm, W. D. Kollmann, H. Krehbiel, and M. Schadlich, Electroproduction of $\pi^+ n$, $\pi^- p$ and $K^+\Lambda$, $K^+\Sigma^0$ final states above the resonance region, Z. Phys. C **3**, 101 (1979).

[115] J. Volmer *et al.*, Measurement of the Charged Pion Electromagnetic Form-Factor, Phys. Rev. Lett. **86**, 1713 (2001).

[116] V. Tadevosyan *et al.*, Determination of the pion charge form-factor for $Q^2 = 0.60$ GeV^2–1.60 GeV^2, Phys. Rev. C **75**, 055205 (2007).

[117] T. Horn *et al.*, Determination of the Charged Pion Form Factor at $Q^2 = 1.60$ and 2.45 $(\mathrm{GeV}/c)^2$, Phys. Rev. Lett. **97**, 192001 (2006).

[118] T. Horn *et al.*, Scaling study of the pion electroproduction cross sections and the pion form factor, Phys. Rev. C **78**, 058201 (2008).

[119] J. Beringer and *et al.* (PDG Collaboration), Review of particle physics, Phys. Rev. D **86**, 010001 (2012).

[120] J. D. Sullivan, One pion exchange and deep inelastic electron-nucleon scattering, Phys. Rev. D **5**, 1732 (1972).

[121] D. Amrath, M. Diehl, and J.-P. Lansberg, Deeply virtual Compton scattering on a virtual pion target, Eur. Phys. J. C **58**, 179 (2008).

[122] M. Diehl, Th. Feldmann, R. Jakob, and P. Kroll, Generalized parton distributions from nucleon form-factor data, Eur. Phys. J. C **39**, 1 (2005).

[123] S.-X. Qin, C. Chen, C. Mezrag, and C. D. Roberts, Off-shell persistence of composite pions and kaons, Phys. Rev. C **97**, 015203 (2018).

[124] J. Rodríguez-Quintero, D. Binosi, C. Mezrag, J. Papavassiliou, and C. D. Roberts, Process-independent effective coupling. From QCD Green's functions to phenomenology, Few Body Syst. **59**, 121 (2018).

[125] D. Binosi, C. Mezrag, J. Papavassiliou, C. D. Roberts, and J. Rodriguez-Quintero, Process-independent strong running coupling, Phys. Rev. D **96**, 054026 (2017).

[126] Z.-F. Cui, J.-L. Zhang, D. Binosi, F. de Soto, C. Mezrag, J. Papavassiliou, C. D. Roberts, J. Rodríguez-Quintero, J. Segovia, and S. Zafeiropoulos, Effective charge from lattice QCD, Chin. Phys. C **44**, 083102 (2020).

[127] Z. Fan and H.-W. Lin, Gluon parton distribution of the pion from lattice QCD, Phys. Lett. B **823**, 136778 (2021).

[128] B. Berthou, D. Binosi, N. Chouika, L. Colaneri, M. Guidal, C. Mezrag, H. Moutarde, J. Rodríguez-Quintero, F. Sabatié, P. Sznajder, and J. Wagner, PARTONS: PARtonic tomography of nucleon software. A computing framework for the phenomenology of generalized parton distributions, Eur. Phys. J. C **78**, 478 (2018).

[129] V. Bertone, S. Carrazza, and J. Rojo, APFEL: A PDF evolution library with QED corrections, Comput. Phys. Commun. **185**, 1647 (2014).

[130] V. Bertone, APFEL++: A new PDF evolution library in C++, Proc. Sci., DIS2017 (**2018**) 201.

[131] B. Pire, L. Szymanowski, and J. Wagner, NLO corrections to timelike, spacelike and double deeply virtual Compton scattering, Phys. Rev. D **83**, 034009 (2011).

[132] H. Moutarde, B. Pire, F. Sabatie, L. Szymanowski, and J. Wagner, On timelike and spacelike deeply virtual Compton scattering at next to leading order, Phys. Rev. D **87**, 054029 (2013).

[133] M. Diehl and D. Yu. Ivanov, Dispersion representations for hard exclusive processes: Beyond the Born approximation, Eur. Phys. J. C **52**, 919 (2007).

[134] C. Mezrag, Ph.D. thesis, IRFU, SPhN, Saclay, 2015.

[135] C. Shi, C. Mezrag, and H.-S. Zong, Pion and kaon valence quark distribution functions from Dyson-Schwinger equations, Phys. Rev. D **98**, 054029 (2018).

[136] R. Abdul-Khalek *et al.*, Science requirements and detector concepts for the electron-ion collider: EIC Yellow report, arxiv:2103.05419.

[137] J. M. Morgado Chávez, V. Bertone, F. De Soto, M. Defurne, C. Mezrag, H. Moutarde, J. Rodríguez-Quintero, and J. Segovia, companion Letter, Accessing the Pion 3D Structure at US and China Electron-Ion Colliders, Phys. Rev. Lett. **128**, 202501 (2022).